Supplementary Materials for:

Impact of material stiffness on the dynamic wetting and deformation of soft matter hemiwicking arrays

Thomas Germain[a,1] **and Shawn A. Putnam**[a,1,2]

[a]University of Central Florida, Mechanical and Aerospace Engineering, Orlando, Florida, 32816, United States of America

This manuscript was compiled on November 2, 2023

This supplementary file includes:

- Supplementary Text (S1–S20)
- Tables S1-S4
- Figures S1–S9
- Captions for Movies S1 and S2
- Legend for Fig. 4 and Fig. 7 [manuscript]
- Nomenclature

Other Supplementary Materials for this manuscript include the following:

- Movies S1 and S2

Both T.G. and S.A.P. designed the experiments, performed research, contributed to sample fabrication, analyzed data, and wrote the paper.

The authors declare no conflict of interest.

[1] T. Germain and S. A. Putnam contributed equally to this work.

[2] To whom correspondence should be addressed. E-mail: shawn.putnam@ucf.edu

Contents

Supplementary Text

S1: Fluids, Materials, and Sample fabrication

The fluids studied include Ethanol (EtOH), Isopropanol (IPA), and Isooctane (IsoO). The key properties of these fluids at room temperature are listed in Table S1.

The materials studied include PDMS (Sylgard 184), Ecoflex^{TM} (Smooth-On, 00-30), PDMS/Ecoflex composites, Norland Optical Adhesive (NOA-61), JB-Weld (Original Cold-Weld), Si wafers, and IP Photoresin (IP-S^2 or IP-L) pillars on Si wafers. Samples were fabricated by either (1) 3D printing at Oak Ridge National Laboratory using the Nanoscribe GT2 (two-photon polymerization) instrumentation or (2) micro-scale lithography replica molding using an in-house stamping/micro-milling apparatus (1).

The hemiwicking samples fabricated by replica molding are continuous materials of either PDMS, Ecoflex, PDMS/Ecoflex composites, NOA-61, or JB-Weld (Table S2). Whereas, the 3D printed hemiwicking samples consist of IP Photoresin pillars on Si wafers coated with protective thin-films of either ∼100 nm of SiO_2 or ∼200 nm of Al_2O_3. The processing conditions for replica molding and the properties of the fabricated wicking arrays are provided in Tables S2–S4.

The replica molding process is rapid, reconfigurable, inexpensive, and adaptable for large-scale manufacturing. To fabricate wicking arrays of different pillar geometries and spacing configurations, negative acrylic molds were first machined by our micro-stamping and micro-milling apparatus (1). Stepper motors control the x- and y-axis spatial placement of the acrylic mold and the z-axis displacement and Θ-rotation/orientation of the micro-machining tool (Fig. S1). A LabVIEW user-control program reads a user-generated bitmap and then mills (or stamps) an acrylic mold according to the setpoint conditions: pillar/cavity location (s_x, s_y), depth ($z_h \rightarrow h$), and overall wicking array dimensions (L, W). Symmetric cylindrical (CYL) pillars are fabricated in drilling mode with a micro end mill, whereas the anisotropic tapered half-cylinder (t,hCYL) pillars are fabricated in stamping mode with a tapered micro milling tool. The resulting pillar geometry (h, r_p, β) is determined by both the cavity depth and the geometry of the micro-machining tool (Fig, 3B [manuscript]). A focused diode laser (3 Watts, $\lambda = 405$ nm) is also used to heat the surface region during cavity fabrication.

For replica molding, uncured sample material is poured onto the negative mold in a fixed height Al mold holder (Fig. S1). The uncured sample is then placed in a vacuum chamber (500 – 850 mbar) to remove residual air pockets in the sample. Then, the samples are cured by either temperature or UV light exposure. For example, the PDMS samples cured (cross-linked) at 100°C for 1 – 5 hours (Table S2), the JB-Weld samples cured at room temperature for 24+ hours, and the NOA-61 samples cured by UV light exposure for 10 – 12 minutes. After curing, the samples are removed from the plastic mold as a hardened substrate material with a microstructured hemiwicking array on one sample surface. The stiffness (Young's modulus, E) of the PDMS samples was controlled by the monomer to cross-linker ratio and curing time (2). The Ecoflex sample (Eco0) and Ecoflex/PDMS hybrid samples (Eco25, Eco50) were fabricated with a similar procedure as that used for PDMS. For the hybrid samples, uncured Ecoflex was mixed with uncured PDMS, and then, underwent the same degassing and curing process (Table S2).

S2: Droplet Wetting Experiments

Droplets are formed by manually ejecting the working fluid from a syringe needle (typically, 31-gauge). The hanging droplets are slowly increased in volume toward a critical droplet volume before depinning/detachment motion from the syringe needle. Then, the droplets are allowed to come into contact with the sample surface (Fig. 1A [manuscript]). The distance between the hanging droplet and the sample surface is forced to be within $10 \sim 100$ μm before contact. The wetting is then with near zero Weber numbers ($We < 10^{-4}$), avoiding any conjugate spreading dynamics tied to the kinetic energy of an impinging droplet (3, 4). The spatiotemporal wetting dynamics are captured with a Phantom high-speed camera with a typical image resolution of 2.067 μm/pixel and frame rate of 21005 fps.

Wetting studies were conducted on the same samples used for the hemiwicking investigations. Some

droplet wetting studies were conducted on the micro-structured regions of hemiwicking samples. However, such studies are rather complicated because they couple the hemiwicking dynamics with inertial wetting dynamics. Therefore, to decouple these dynamics, the results discussed herein (and in the main manuscript) only pertain to inertial wetting and spreading on the flat, non-structured sample surface regions.

The data provided in Fig. 1*D*–*F* [manuscript] plots the averaged droplet wetting results from multiple trials using the conventional scaling for inertial wetting (5–8):

$$r(t)/R \approx t\,/\sqrt{(\rho/\gamma)R^3}, \qquad \text{[S1]}$$

where R is the droplet radius before contact, ρ is the fluid density, and γ is the surface tension of the fluid. The corresponding mean and standard error in this $r(t)/R$ data are based on $N = 4 \pm 1$ droplet wetting trials using different, non-textured sample surface regions. For data analysis of each wetting trial, we used both imaged sides of the spreading droplet at the solid-liquid-vapor triple-line. For ease in viewing, only the maximum error for each sample-fluid couple is displayed in Fig. 1*D*–*F* [manuscript]. To highlight the trial-by-trial variation in the wetting dynamics, Fig. S2*A* and S2*B* provide the wetting data from multiple trials with Eco0-IPA and Eco0-IsoO, respectively. These results also emphasized the unique droplet wetting dynamics observed with swelling fluids (e.g., IsoO) on the ultrasoft Eco0 ($E \sim$61 kPa) sample. Aside from the unique Eco0-IsoO results, the stiffness (Young's modulus, E) of the sample substrate had no notable effect on the inertial wetting dynamics.

Fig. 2 [manuscript] plots the maximum wetting velocities ($\hat{\mathrm{v}}_{\mathrm{wet}}$) attained from our spatiotemporal droplet wetting experiments (Fig. 1*D*–*F* [manuscript]). These measured $\hat{\mathrm{v}}_{\mathrm{wet}}$ values are based on evaluating the wetting rate dr/dt at $r \approx 100$ μm (or $r/R \approx 0.1$) for each respective sample-fluid couple. The corresponding standard error in $\hat{\mathrm{v}}_{\mathrm{wet}}$ measured is simply based on evaluation of $\Delta(dr/dt)$. Fig. 2 [manuscript] also compares $\hat{\mathrm{v}}_{\mathrm{wet}}$ measured to that predicted (Eq. 2 [manuscript], Eq. S2a), where both θ_{Eq} and x_0 are measurable quantities. The predicted error in $\hat{\mathrm{v}}^{\mathrm{p}}_{\mathrm{wet}}$ (Eq. S2a) is therefore the propagated error from $\Delta(\theta_{\mathrm{Eq}})$ and $\Delta(x_0)$. More details on the characterization of θ_{Eq} and x_0 are provided in Sec. S3 and S4. Table S3 also lists the mean and standard errors measured for $\hat{\mathrm{v}}_{\mathrm{wet}}$, θ_{Eq}, x_0, and the incident $R \pm \Delta R$ droplet radii.

We point out that aside from the $\cos(\theta_{\mathrm{Eq}}/2)$ term and the use of x_0, Eq. S2a (or Eq. 2 [manuscript]) is identical to that derived for bubble coalescence (9, 10). Perhaps the width of the capillary neck (w_0) should be used rather than x_0 in Eq. S2a – especially for predicting the maximum wetting speeds of tiny droplets ($R \lesssim x_0$). Yet, the intrinsic w_0 width at the onset of droplet wetting is very difficult to quantify and the correlation between $\hat{\mathrm{v}}_{\mathrm{wet}}$ measured and that predicted by Eq. S2a is very good using x_0. Moreover, we have found from a series of preliminary, high-magnification droplet wetting experiments with various sample-fluid couples and moderately-sized droplets ($R > 200$ $\mu\mathrm{m} \gg x_0$) that w_0 appears to be within the narrow range of $2 \sim 30$ μm (i.e., w_0 values comparable to x_0 measured with our micropillar hemiwicking arrays).

As a preliminary assessment of viscoelastic dampening of $\hat{\mathrm{v}}_{\mathrm{wet}}$, below we reproduce Eq. 2 [manuscript] along with our expectations based on elastocapillary storage (Eq. S2b).

$$\hat{\mathrm{v}}^{\mathrm{p}}_{\mathrm{wet}} \approx \sqrt{2\gamma\cos(\theta_{\mathrm{Eq}}/2)\,/\rho\,x_0} \qquad \text{[S2a]}$$

$$\hat{\mathrm{v}}^{\mathrm{ec}}_{\mathrm{wet}} \approx \left[\frac{2}{\rho}\left(\frac{\gamma\cos(\theta_{\mathrm{Eq}}/2)}{x_0}\right) - \frac{2}{\rho}\left(\frac{8\gamma^2(1+\nu)^2}{E\,x_0^2}\right)\right]^{1/2} \qquad \text{[S2b]}$$

As addressed in the main manuscript, Eq. S2a is derived from the energy balance: $\rho\mathrm{v}^2/2 \approx \gamma\cos(\theta_{\mathrm{Eq}}/2)\,/x_0$, where $\rho\mathrm{v}^2/2$ is the change in the kinetic energy per unit volume of the fluid (immediately after droplet-surface contact) and $\gamma\cos(\theta_{\mathrm{Eq}}/2)\,/x_0$ is the change in the potential energy of the droplet (contact to static equilibrium). Eq. S2b accounts for the viscoelastic energy that is temporarily stored in the wetted substrate (per unit volume) – i.e., the second parentheses term, where $u_{\mathrm{ec}} = \frac{1}{2}E\epsilon_{\mathrm{ec}}^2$ is energy density stored until elastic recoil for an equivalent elastocapillary strain of $\epsilon_{\mathrm{ec}} \approx 2l_{\mathrm{ec}}/x_0 \approx 4\gamma(1+\nu)/E\,x_0$ (see, Eq. S28–S29c). We note that Eq. S2b predicts reduced maximum wetting velocities of reasonable values; however, these

predicted $\hat{v}_{wet}^{ec}$ values are still considerably larger than $\hat{v}_{wet}$ measured for Eco0-IPA and Eco0-IsoO (Fig. 1 [manuscript], Fig. S3). Moreover, Eq. S2b does not account for swelling effects. Therefore, we leave the application of Eq. S2b (and refinements thereof) for future studies.

S3: Contact angle measurements

The advancing θ_{Adv}, receding θ_{Rec}, and equilibrium θ_{Eq} contact angles of the different sample-fluid couples were measured using a simple goniometer setup. The setup is identical to that used for the inertial wetting (Fig. S3, Fig. 2*A* [manuscript]). For example, θ_{Adv} and θ_{Rec} were measured via the contemporary approach of videography during respective fluid dispensing and then fluid withdrawal between the droplet and syringe needle. Whereas, θ_{Eq} was measured after dispensing without droplet-needle contact. Similar to the inertial wetting studies, each contact angle measurement trial used a different non-structured surface region on the sample. For example, $N \geq 3$ surface regions were tested, yielding 6^+ dynamic (θ_{Adv}, θ_{Rec}) and 6^+ static (θ_{Eq}) contact angle measurements. Table S3 lists the θ_{Eq} results. Fig. S3 also plots the θ_{Eq} results, along with θ_{Adv} and θ_{Rec} measured for all systems studied herein.

S4: Meniscus extension measurements

The equilibrium meniscus extension (x_0) is a key property used to estimate multiple dynamic processes tied to the propagation of the solid-liquid (meniscus) interface, including (1) the droplet wetting dynamics (Eq. S2a, Eq. 2 [manuscript]), (2) the spatiotemporal hemiwicking dynamics (Eq. S8–S16, Eq. 3–7 [manuscript]), and (3) the transient deflection of the micropillars during hemiwicking (Eq. S17–S19b, Eq. 9 [manuscript]). The meniscus extension is characterized by a combined interferometry and videography measurement technique that is conducted during the steady-state mode of the working fluid evaporation in the hemiwicking array (11). For example, after completion of the hemiwicking process, the meniscus extension from the last row of pillars in the wicking array remains constant as the evaporation rate is balanced with the mass flow rate from the fluid pool reservoir ($\dot{m}_{evap} = \dot{m}_{wick}$). This steady-state x_0 imaging and measurement methodology is illustrated in Fig. S4 (see also Figs. 1 and 3 in Refs. (12) and (13), respectively).

Tables S3 and S4 list x_0 measured for all studied sample-fluid couples. For the lyophilic systems studied herein, $\theta < 60°$ and x_0 is typically observed within the narrow range of $20 \sim 30$ μm. Exceptions include, the slightly reduced $x_0 \approx 15 \sim 20$ μm values for the SiO_2 coated CYL pillar arrays and the abnormally extended $x_0 > 50$ μm values with the anisotropic (t,hCYL) JB-Weld and NOA-61 wicking arrays.

We have some ideas on how to predict x_0 from first principles. But, this will addressed in future studies. Herein we only demonstrate how x_0 can be estimated from our inertial wetting results. For example, rewriting Eq. S2a as $x_0 = \frac{2\gamma\cos(\theta_{Eq}/2)}{\rho\,\hat{v}_{wet}^2}$ facilitates calculation of x_0 from our corresponding $\hat{v}_{wet}$ and θ_{Eq} measurements. Fig. S5 shows the notable correlation between x_0 measured by meniscus imaging and x_0 calculated from Eq. S2a with our coexisting $\hat{v}_{wet}$ and θ_{Eq} results.

S5: Young's modulus characterization

A simple cantilever beam bending setup is used to measure the stiffness (Young's modulus, E) of the PDMS, Ecoflex, Ecoflex/PDMS composite, NOA61, and JBweld samples (Fig. S6*A*). Each sample was first cut into the shape of a rectangular bar. Then, clamped (fixed) at one end and subjected to different force (mass) at the free end of the sample (e.g., 0.2 – 20 grams). A camera measured the corresponding sample/beam deflection for a given mass (force) relative to the sample without added mass (Fig. S6*B*). Knowing the force, deflection, and sample geometry, the Young's modulus is calculated from:

$$E = \frac{F}{6 I_x \delta_{\hat{y}}}\left[c^2(3L_s - c)\right], \qquad [S3]$$

where L_s is the free length of the clamped sample, $F = mg$ is the applied force for a given mass, c is the distance of the mass (center) from the clamped end of the sample ($c \leq L_s$), $\delta_{\hat{y}}$ is the measured, maximum

y-axis deflection of the free end of the sample for a given load, and I_x is area moment of inertia of cross section. For a rectangular bar, $I_x = ab^3/12$, where a and b are the width and thickness (respectively). Neglecting the Poisson effect, the bending modulus is the product $E\,I_x$. Table S3 lists the E results based on multiple trials ($N > 2$) per applied mass. The PDMS–Ecoflex trials used masses of 0.2, 0.5, 0.7, 1.0, 1.2, 1.5, and 2.0 grams. The NOA61 and JBweld trials used masses of 2, 5, 7, 10, 15, and 20 grams.

S6: Effective Young's Modulus of coated IP photoresin pillars on Si wafers

The 3D printed hemiwicking samples are IP Photoresin (IPP) pillars on silicon (Si) wafers. For protection and surface energy homogenization, the samples/pillars were coated with thin-films of SiO_2 or Al_2O_3. The effective Young's modulus of these thin-film coated pillars are calculated based on

$$E_\Phi = \frac{E_p}{(1+\Phi)^3}\left(1+\zeta\Phi\left[\Phi^2+3\frac{(1+\Phi)^2}{1+\zeta\Phi}\right]\right). \quad [S4]$$

Eq. S4 is based on Eq. 9 in Ref. (14), where $\Phi = t_\mathrm{f}/\bar{r}_p$, $\zeta = E_\mathrm{f}/E_p$, t_f is the coating thickness, $\bar{r}_p$ is the height-weighted pillar radius, E_f is the modulus of the thin-film coating, and E_p is the modulus of the IPP pillar core material. The calculated E_Φ values are listed in Table S4, where $t_{SiO_2} \approx 100$ nm, $t_{Al_2O_3} \approx 200$ nm, $E_{SiO_2} \approx 73$ GPa, $E_{Al_2O_3} \approx 200$ GPa, and $E_\mathrm{IPP} \approx 4.5 \pm 0.6$ GPa.

S7: Vertical hemiwicking experiments

Vertical hemiwicking experiments were conducted by translating a fluid pool reservoir against gravity into hemiwicking array (Fig. 3*A* [manuscript]). The fluid reservoir is raised until the free surface pool reaches the first few rows of pillars in the wicking array. The motion of the fluid was captured using both a Point Grey flea camera (Resolution = 4.14 μm/pixel, Frame Rate = 50 fps) and a Phantom high-speed camera with image resolutions within $3.823 \sim 19.86$ μm/pixel (most frequently, 19.86 μm/pixel) and frame rates within $100 \sim 11000$ fps (most frequently, 100 fps). The same method was used to obtain the initial hemiwicking velocity ($\hat{\mathrm{v}}_\mathrm{onset}$, Fig. 5*A*,*E* [manuscript]). However, $\hat{\mathrm{v}}_\mathrm{onset}$ was captured at increased frame rates and image resolutions (Frame Rate = $7500 \sim 11001$ fps, Resolution = 0.847 μm/pixel), where the image resolution is adjusted by simple replacement/exchange of the infinity-corrected, long working distance microscope objective on the compound imaging setup.

The hemiwicking results provided in Fig. 4*A*–*F* [manuscript] are the averaged data from multiple experiments ($N = 7 \pm 4$) by spline interpolation. For ease of viewing, only the maximum standard error in the wicking velocity (v) is provided for each sample-fluid couple. The experimental trial-by-trial variations in the measured hemiwicking results are due to mainly (i) physical and chemical degradation of the wicking samples and (ii) systematic experimental errors. The latter is primarily due to experimental variations in the distance between the free surface of the pool reservoir and the beginning of the wicking array. For example, the initial hemiwicking velocity can be significantly reduced if the pool surface (or starting wetting front) is not in direct (or uniform) contact with the first row of pillars. As opposed to horizontal hemiwicking studies (wicking flow perpendicular to gravity), vertical hemiwicking studies were conducted because they had reduced systematic experimental error associated with the initial wetting of the beginning of the wicking array. For vertical hemiwicking, we minimized this systematic error by using a stage stop to limit the maximum vertical displacement of the pool stage (Fig. 3*A* [manuscript]). In regards to physical and chemical degradation of the wicking arrays, the soft matter PDMS and Ecoflex/PDMS hemiwicking samples were the most robust. For example, the wicking data for the PDMS, Ecoflex/PDMS, NOA61, and JBweld samples are based on experiments that spanned over the course of almost two years of testing. Whereas, the protective-coated (Al_2O_3 or SiO_2) IPP pillar arrays on Si started to physically and chemically degrade after a couple months of testing.

S8: Derivation of the 1D, fully developed hemiwicking velocity: $\mathrm{v}(\ell)$

The hemiwicking model described herein (and briefly in the main manuscript) predicts the 1D wicking velocity (v) of the working fluid as a function of the meniscus propagation distance (ℓ) from a free surface pool. Similar to other hemiwicking models in the literature (15–20), the derivation is based on a simple force (or energy) balance between the capillary pumping/wicking force and fluid viscous drag force. We note that the model presented herein is a revised version of that tested previously with different fluids and symmetric (12) and anisotropic (13, 21) pillar arrays coated with various materials. Thus, the model accommodates wicking velocity predictions with wicking arrays having both symmetric (cylinder: CYL) and asymmetric (half-conical: hCONL, tapered, half-cylinder: t,hCYL) pillar geometries, along with wicking arrays of both staggered ($\alpha \neq 0°$) and rectangular/cubic pillar placements ($\alpha = 0°$). Fig. 3*B* [manuscript] depicts a wicking array of length (L) and width (W) of anisotropic, hCONL pillars orientated in a 2D staggered-rectangular-lattice (srl) unit cell configuration ($s_x \neq s_y$, $\alpha \approx 40°$). Also see Fig. S1 and Fig. 1–3 in Ref. (13) for examples of other sample geometries and wicking configurations.

The hemiwicking flow in a micropillar array from a free surface pool is in the Stokes flow regime ($\mathrm{Re} \ll 1$) with a resistive drag force $F_{C_d} \propto \mu \bar{\mathrm{v}} L_c$. The drag force for vertical hemiwicking is based on the accumulative drag from the pillar walls, where both the base wall surface drag and unsteady viscous dissipation effects are neglected (12, 13, 21). Our model derivation of $\mathrm{v}(\ell)$ is conducted using a per unit wicking cell convention. In result, the drag force per unit cell width normal to the flow along the x-axis is

$$f_{C_d} \approx \frac{1}{2} \rho \, \bar{\mathrm{v}}^2 C_d \left(\frac{A_{C_d}}{s_x s_y} \right) \ell_x, \qquad \text{[S5]}$$

where C_d is the drag coefficient, A_{C_d} is the frontal drag area per unit wicking cell and $\bar{\mathrm{v}}$ is average wicking front velocity in the wicking cell located at a distance ℓ_x from the free surface pool. If the free surface pool is positioned at the beginning of the wicking array ($\ell_x/L = 0$), then the number of wicked pillars per unit cell width at ℓ_x is $N_p = (1/s_x)\,\ell_x$ and the net viscous drag area per unit cell width at ℓ_x is $N_p\,(A_{C_d}/s_y)$.

If the drag coefficient (per unit wicking cell) is estimated as $C_d = C_{d0}/\mathrm{Re}_{L_c}$, then the drag force per unit wicking cell width (Eq. S5) reduces to

$$f_{C_d} = \frac{1}{2} \bar{\mathrm{v}} \, C_{d0} \, \frac{\mu}{L_c} \left(\frac{A_{C_d}}{s_x s_y} \right) \ell_x \qquad \text{[S6]}$$

where we also use $C_{d0} = 24$ for creeping Stokes flow and, for reference, $\mathrm{Re}_{L_c} = \rho \bar{\mathrm{v}} L_c / \mu$.

The wicking/pumping force (per unit wicking cell) can be evaluated based on the conventional capillary rise problem, where each wicking cell (pillar) acts as a fluid pump with a pumping pressure (per unit wicking cell) scaling as $\delta P \approx \gamma \kappa$. The wicking force per unit cell width normal to the flow along the x-axis is

$$f_w = \gamma \, \kappa \left(\frac{A_w}{s_y} \right) \approx \gamma \left[\frac{\cos \theta_{\mathrm{Eq}}}{s_\kappa} \right] \left(\frac{A_w}{s_y} \right), \qquad \text{[S7]}$$

where γ is the surface tension of the fluid, κ is the average spatiotemporal curvature of the propagating meniscus (for x-axis flow), and the ratio A_w/s_y is the pumping area per unit wicking cell width. In Eq. S7, the average meniscus curvature is estimated as $\kappa \approx [\cos(\theta_{\mathrm{Eq}})/s_\kappa]$, where θ_{Eq} is the equilibrium contact angle with the non-structured (flat) surface material (i.e., the intrinsic θ_{Eq} for each sample-fluid couple) and s_κ is the inter-pillar gap separation (i.e., the minimum separation between neighboring pillars).

A force balance $f_{C_d} = f_w$ (i.e., equating Eq. S6 with the right hand side of Eq. S7) with subsequent algebraic manipulation in terms of $\bar{\mathrm{v}}$, leads to:

$$\bar{\mathrm{v}}(\ell_x) = \frac{(\gamma/\mu)}{C_{d0}} \left(\frac{1}{\ell_x} \right) K_x = \frac{(\gamma/\mu)}{C_{d0}} \left(\frac{1}{\ell_x} \right) \left[\frac{2 \cos \theta_{\mathrm{Eq}}}{s_\kappa} \left(\frac{A_w}{A_{C_d}} \right) L_c \, s_x \right]. \qquad \text{[S8]}$$

The predicted hemiwicking velocity solution (Eq. S8) scales as $1/\ell$. The first part of Eq. S8 is written in its compact form and is identical to Eq. 3 [manuscript], where $\mathrm{v_{Ca}} = (\gamma/\mu)$ is the capillary velocity, C_{d0} is the Stokes drag coefficient, and K_x is the solid-liquid surface texture (for x-axis flow). The bracketed term on the right-hand-side of Eq. S8 is the generalized solution for K_x, where the ratio, $S = K/\ell$, is a dimensionless quantity called the solid-liquid Structure factor that represents the hemiwicking efficiency ($0 \leq S \leq 1$) for $\ell >> K$. Both S and K are analogous to a Structure factor and surface roughness in materials science; however, both these parameters couple the fluid's meniscus curvature to the 2D packing configuration and pillar geometry of the wicking array (Fig. 3*B* [manuscript]).

To account for both the packed bed limit ($s_\kappa/s_x \to 0$) and closely packed wicking array configurations ($s_\kappa < x_0$), both s_κ and s_x in Eq. S8 should be replaced by $s_\kappa^* = \max[s_\kappa, x_0]$ and $s_x^* = \min[s_\kappa, s_x - \bar{r}_p]$, respectively. We also note that the characteristic length (L_c) in Eq. S8 was previously estimated based on the pillar geometry (12, 13). For example, $L_c = 2r$ and $L_c = r$ for CYL and hCONL pillars, respectively. However, hemiwicking flow actually resembles that of open channel flow. Therefore, L_c is more appropriately defined as the hydraulic radius per unit wicking cell for open channel flow (R_h^{ocf}).

Based on these considerations, the solid-liquid Surface texture in Eq. S8 for 1D hemiwicking flow along the x-axis is defined as

$$K_x = 2\left(\frac{\cos(\theta_{\mathrm{Eq}} + \beta)}{s_\kappa^*}\right)\left(\frac{A_w}{A_{C_d}}\right) R_h^{\mathrm{ocf}} s_x^* \,, \qquad \text{[S9]}$$

where the inter-pillar gap separation is refined as $s_\kappa^* = \max[s_\kappa, x_0]$ to account for arrays with pillar separations less than the equilibrium meniscus extension, $s_x^* = \min[s_\kappa, s_x - \bar{r}_p]$ accounts for the packed-bed limit using the height-weighted average pillar radius ($\bar{r}_p$), the meniscus pumping area to drag area ratio is $A_w/A_{C_d} \approx 1$, and the meniscus curvature contribution ($\kappa = \cos(\theta_{\mathrm{Eq}} + \beta)/s_\kappa^*$) has the added β slant angle term to account for hemiwicking with pillar walls that are slanted relative to the substrate surface normal.

Like that for K (Eq. 4 [manuscript]), Eq. S9 is a generalized solution for the solid-liquid Surface texture. Thus, all parameters in Eq. S9 (aside from θ_{Eq}) are dependent on not only the wicking array geometry, but also the flow field propagation direction relative to the pillar geometry/orientation in the unit wicking cell. For example, for symmetric CYL pillars, $\beta = 0°$; for symmetric CONL (or t,CYL) pillars, $\beta > 0°$; and for anisotropic hCONL and t,hCYL pillars, $\beta = 0°$ for the faster (Rapid Ascent, RA) hemiwicking direction and $\beta > 0°$ for the reversed, opposite and slower (Sluggish Climb, SC) wicking direction (Fig. 3*B* [manuscript]; see also Fig. S10 in Ref. (21)).

For the different CYL, hCONL, and t,hCYL wicking arrays studied herein, the corresponding inter-pillar gap separations (s_κ – equations) to be used in Eq. S8 and S9 are:

$$s_\kappa|_{\mathrm{CYL}} = s_x/\cos\alpha - 2r_p \qquad \text{[S10a]}$$

$$s_\kappa|_{\mathrm{t,hCYL}} = \sqrt{(s_y/2 - r_p)^2 + (s_x/2 - r_p)^2} \qquad \text{[S10b]}$$

$$s_\kappa|_{\mathrm{hCONL}} = \sqrt{(s_y/2 - r_p)^2 + (s_x/2 - r_p)^2}\,. \qquad \text{[S10c]}$$

Fig. S7 plots the calculated K values for all the sample-fluid couples studied. A comprehensive listing of all hemiwicking sample properties, pillar geometries, and corresponding model parameters are also listed in Table S4. The Supplementary Nomenclature section also provides a listing of all the model variables and parameters used above – along with those addressed in the main manuscript and those addressed hereafter.

S9: Hydraulic radius (per unit wicking cell) for open channel flow: R_h^{ocf}

The characteristic length $L_c = R_h^{\mathrm{ocf}}$ of the hemiwicking flow is needed for calculation the solid-liquid K surface texture (Eq. S9, Eq. 4 [manuscript]). This characteristic length based on the hydraulic radius for open channel hemiwicking flow is calculated via $R_h^{\mathrm{ocf}} = (A_c^{\mathrm{flow}}/\mathcal{P}_{\mathrm{wet}})\cos\alpha$, where A_c^{flow} is the frontal area for fluid flow per unit wicking cell, $\mathcal{P}_{\mathrm{wet}}$ is the wetted perimeter per unit cell, and the additional $\cos\alpha$ term has been included to the traditional R_h^{ocf} definition to account for staggered pillar placements. For

the different CYL, hCONL, and t,hCYL wicking arrays, the corresponding R_h^{ocf} expressions to be used in Eq. S8 and S9 are

$$R_h^{\text{ocf}}|_{\text{CYL}} = \frac{h(s_y - 2r_p)}{2h + (s_y - 2r_p)} \cos\alpha \quad \text{[S11a]}$$

$$R_h^{\text{ocf}}|_{\text{t,hCYL}} = \frac{h(s_y - 2r_p + h\tan\beta)}{2(h/\cos\beta) + (s_y - 2r_p)} \cos\alpha \quad \text{[S11b]}$$

$$R_h^{\text{ocf}}|_{\text{hCONL}} = \frac{h(s_y - r_p)}{2(h^2 + r_p^2)^{1/2} + (s_y - 2r_p)} \cos\alpha. \quad \text{[S11c]}$$

S10: Entrance length and Maximum wicking velocity predictions

As revealed by the hemiwicking model predictions in Fig. 4 [manuscript], Eq. S8 over predicts the wicking velocities at the onset of hemiwicking. This is because the model derivation (Eq. S5–S8) is based on the force balance $f_w \approx f_{C_{d0}}$ for $\ell/s_x \gg 1$ (or $\ell/K > 1$) – i.e., the steadily increasing viscous dissipation regime where both the unsteady inertial effects and the flow-field entrance dynamics can be neglected. Therefore, in analogy with the developing-to-developed flow-field dynamics in a pipe, the hemiwicking front must also propagate a given entrance length (ℓ_e) before *developed 1D hemiwicking flow* can be established. Furthermore, if ℓ_e is known, then the maximum (apex) wicking velocity in the wicking array at $\ell = \ell_e$ should simply follow from Eq. S8 as

$$\hat{\text{v}}_{\text{wick}} = \frac{\text{v}_{\text{Ca}}}{C_{d0}} \frac{K}{\ell_e}. \quad \text{[S12]}$$

Traditionally, the entrance length for fully developed laminar flow in a pipe is calculated based on $\ell_e \approx 0.065 D_h \text{Re}$, where D_h is the hydraulic diameter of the pipe and Re is the corresponding Reynolds number for the flow at the pipe inlet from a pressure reservoir. However, for hemiwicking flow, the flow-field in the wicking array is driven by the cascade of inter-pillar capillary pumping/actions inside the wicking array (i.e., the flow is internally driven), whereas channel (or pipe) flow is externally driven by a commonly constant pressure source (i.e., flow via a pressure reservoir). Nevertheless, in analogy with laminar channel flow, the hemiwicking entrance length is evaluated as

$$\ell_e = 0.065\, L_c^{\text{pool}}\, \text{Re},$$

$$\ell_e = 0.065\, L_c^{\text{pool}} \left[\frac{\hat{\text{v}}_{\text{wet}} R_h^{\text{ocf}}}{\mu/\rho}\right], \quad \text{[S13]}$$

where L_c^{pool} is the characteristic hydrodynamic boundary length of the pool reservoir and the bracketed term is the corresponding inlet Reynolds number per unit wicking cell for open channel hemiwicking flow. As shown in Eq. S13, this inlet Reynolds number at the onset of hemiwicking flow is evaluated based on the maximum speed $\hat{\text{v}}_{\text{wet}}$ for wetting the sample surface (Eq. S2a), the kinematic viscosity of the fluid (μ/ρ), and the hydraulic radius R_h^{ocf} for open channel flow per unit wicking cell (Eq. S11a–S11c).

The application of Eq. S13 for subsequent $\hat{\text{v}}_{\text{wick}}$ predictions with Eq. S12 still requires knowledge of L_c^{pool}. The volume of displaced fluid in the pool reservoir must scale proportionally with the volume of wicked fluid. Therefore, L_c^{pool} can be calculated from a simple volume flow rate balance between the flow rate at L_c^{pool} in the pool reservoir and the flow rate in the wicking array after the onset of hemiwicking:

$$\dot{V}_{\text{pool}} = \dot{V}_{\text{wick}},$$

$$\bar{\text{v}}_{\text{pool}} \cdot A_c^{\text{pool}} = \bar{\text{v}}_{\text{wick}} \cdot A_c^{\text{wick}}. \quad \text{[S14]}$$

For hemiwicking from a partially patterned, flat wall substrate (Fig. 3*A,B* [manuscript]), the cross-sectional areas (A_c^{pool}, A_c^{wick}) in Eq. S14 can be expressed in terms of L_c^{pool} and the geometrical configuration of wicking array. This allows L_c^{pool} to be calculated from the resulting quadratic solution:

$$\bar{\text{v}}_{\text{pool}} \left[\pi L_c^2 + \frac{\pi}{2} L_c W\right] = \bar{\text{v}}_{\text{wick}} \left[\sqrt{2}\, x_0 W (1 - \phi_{A_F})\right], \quad \text{[S15]}$$

where $(1-\phi_{A_F})$ is the frontal area flow fraction in the wicking array, W is the width of the wicking array, and $\sqrt{2}\,x_0$ is the interfacial length of the propagating meniscus. A solution for L_c^{pool} via Eq. S15 can be easily found after recognizing that the pool's flow-field perturbation at L_c^{pool} requires satisfaction of the traditional the boundary layer velocity condition: $\bar{\text{v}}_{\text{pool}}|_{@L_c} = 0.01\bar{\text{v}}_{\text{wick}}$. Eq. S15 then simplifies to

$$\left[\pi L_c^2 + \frac{\pi}{2} L_c W\right] = \frac{1}{0.01}\left[\sqrt{2}\,x_0 W(1-\phi_{A_F})\right]. \qquad \text{[S16]}$$

The calculated value of L_c^{pool} via Eq. S16 can now be used to calculate the entrance length (ℓ_e, Eq. S13) and, then subsequently, the maximum (apex) hemiwicking velocity ($\hat{\text{v}}_{\text{wick}}$, Eq. S12). It turns out that the correlation between $\hat{\text{v}}_{\text{wick}}$ measured and that predicted (via Eq. S12–S16) is actually quite good – typically within $10 \sim 50\%$ (Fig. 4*D–F* and Fig. 5*G,H* [manuscript]). We note that aside from the coupled sample-fluid meniscus extension x_0 property, L_c^{pool} (via Eq. S16) is independent of all other properties of the working fluid (γ, ρ, μ). As a result, the calculated L_c^{pool} values end up being within the fairly narrow range of $L_c^{\text{pool}} = 0.68 \pm 0.19$ mm for all sample-fluid couples studied herein. It is also noted that using L_c^{pool} instead of ℓ_e in Eq. S12 leads to only fair predictions of $\hat{\text{v}}_{\text{wick}}$ with the EtOH working fluid (i.e., this substitution significantly underpredicts $\hat{\text{v}}_{\text{wick}}$ for IPA and significantly overpredicts $\hat{\text{v}}_{\text{wick}}$ for IsoO).

S11: Critical imbibition criterion

The recent hemiwicking studies by Natarajan et al. (20) accommodated for enhanced viscous drag from the microtexture and reduced wicking speeds via a critical imbibition criterion. This criterion effectively predicts a wicking velocity that scales as $\text{v} \propto C_w(\frac{\gamma}{\mu})\frac{h}{x_0}\frac{1}{C_d}$, where $C_w = (\cos\theta - \cos\theta_c)\,/\,\cos\theta_c$ is the hemiwicking (imbibition) coefficient, θ is the equilibrium (or advancing) contact angle, and θ_c is the critical contact angle for hemiwicking (imbibition) for a given sample-fluid chemistry couple and pillar geometry-spacing configuration. Thus, for hemiwicking to occur $\theta < \theta_c$ (or $C_w > 0$) is required, where the wicking speed is bound by the upper-limit capillary velocity $\text{v}_{\text{Ca}} = (\gamma/\mu)$. For this work, the range of this imbibition coefficient is restricted to $0 \leq C_w \leq 1$, yielding a universal critical contact angle of $\theta_c \approx 60°$. This universal $\theta_c \approx 60°$ value corresponds quite well with our observations (i.e., hemiwicking was not observed for other tested sample-fluid couples with $\theta_{\text{Adv}} > 60°$). Nevertheless, the fluid-soft matter combinations studied herein have corresponding C_w values that range within approximately $0.33 \lesssim C_w \lesssim 0.99$, using $\theta_c = 60°$ and the measured values of θ_{Eq} and θ_{Adv} (Fig. S3). We note that earlier work by Krishnan et al. (12) also accommodated for wicking speed variations (for a given fluid and pillar geometry-spacing configuration), but instead used a fitted drag coefficient that was always greater than the theoretical value for creeping Stokes flow (i.e., $C_{d0}^* > C_d^{\text{Stokes}}$). For reference, the predicted wicking velocity in (12) scales as $\text{v} \propto (\frac{\gamma}{\mu})\frac{h(s-2r)}{x_0^2}\frac{1}{C_{d0}^*}$, where $(s-2r)$ is the pillar-to-pillar wall separation for a CYL pillar array.

S12: Critical modulus for pillar clustering

The critical modulus for pillar clustering during hemiwicking and evaporation is calculated using a cantilever beam deflection model for a partially distributed load:

$$\delta_{\max} = \frac{\bar{w}}{24EI_y}\left[4h(z^3 - \Delta_z^3) - (z^4 - \Delta_z^4)\right], \qquad \text{[S17]}$$

where $\delta_{\max}$ is the maximum deflection length of the tip of the pillar, $\bar{w}$ is the average load distribution [N/m], h is the pillar height, z is the pillar wetting height ($x_0 \leq z \leq h$), $\Delta_z = (z - x_0)$ is the region for the capillary bending forces relative to the meniscus x_0 extension, and I_y is the area moment of inertia of cross section for the pillar for x-axis hemiwicking flow. The calculated I_y values for the different wicking arrays (pillar geometries) are listed in Table S4. For reference, $I_y = \frac{\pi}{4}r_p^4$ for CYL pillars.

At the beginning of the drying (evaporation) process, the pillar walls in the hemiwicking array are completely wetted ($z = h$). Then, as the fluid evaporates, the meniscus curvature increases as $\kappa(t) \approx 2\cos\theta(t)/s_\kappa$ until $\theta(t) \approx \theta_{\text{Rec}}^*$, where θ_{Rec}^* is the apparent receding contact angle with the pillar walls.

Therefore, during the evaporation process, the average bending load distribution over the meniscus extension region should scale as

$$\bar{w} = \frac{2\gamma \cos\theta^*_{\text{Rec}}}{s_\kappa} \left(2\bar{r}_p\right), \qquad \text{[S18]}$$

where s_κ is the inter-pillar gap separation (Eq. S10a–S10c), $\theta^*_{\text{Rec}} \approx \theta_{\text{Rec}}$, and θ_{Rec} is the receding contact angle measured for the non-textured region of the sample-fluid couple (Fig. S3).

S12A: Pillar clustering should certainly occur when $\delta_{\max} > s_\kappa/2$. However, as any two or more pillars deflect toward each other, the meniscus curvature also increases such that the average bending load increases as $\bar{w}(\delta_{\hat{p}}) \propto \gamma/(s_\kappa - \delta_{\hat{p}})$. Thus, any inter-pillar deflection beyond a threshold $\delta_{\hat{p}}$ can induces a cascade of pillar clustering events (Movie S2). Using Eq. S17 with $\delta_{\max} = s_\kappa/2$ and Eq. S18 for $\bar{w}$, the critical modulus for clustering of CYL pillars during wicking array evaporation is

$$E_{\text{cr}} = \frac{4\gamma \cos\theta_{\text{Rec}}}{3\pi \bar{r}_p^3 s_\kappa^2} \left[3h^4 - 4h\Delta_h^3 + \Delta_h^4\right], \qquad \text{[S19a]}$$

$$E^*_{\text{cr}} = \frac{4\gamma \cos\theta_{\text{Rec}}}{3\pi \bar{r}_p^3 s_\kappa^2} \left[3h^4 - 4h\Delta_h^3 + \Delta_h^4\right] \times \mathcal{S}_r^2, \qquad \text{[S19b]}$$

where $\Delta_h = (h - x_0)$ is the meniscus region for the capillary bending forces during evaporation and $\mathcal{S}_r$ is the swelling ratio for a given sample-fluid couple.

S12B: We have included Eq. S19b in addition to Eq. S19a to specifically address the effects of swelling-induced softening of the micropillars. Initially, we found from data analysis a $E^*_{\text{cr}} \propto \mathcal{S}_r^2$ dependence. However, after review of the pioneering work of Paul J. Flory (22–24), we found that Flory actually predicted elastic modulus softening to the five-thirds power of the volume swelling ratio. For example, swelling of a cross-linked polymer from its initial dry state (E_0, V_0) to its final equilibrium swelled state $(E_{\mathcal{S}}, V/V_0 = \mathcal{S}_r^3)$ causes a elastic modulus softening that scales as $E_{\mathcal{S}} \approx E_0/\mathcal{S}_r^5$ (see also Eq. S44 and the corresponding discussion thereof in Sec. S17). In terms of Eq. S19b, along with swelling-induced softening of the micropillars, there is also radial swelling (expansion) of the micropillars: $r_p \approx r_{p_0}\mathcal{S}_r$. Therefore, the revised dry state critical modulus for CYL pillar clustering is $E^*_{\text{cr}} \approx E_{\text{cr}} \times \mathcal{S}_r^2$, where E_{cr} represents the expected modulus for clustering in the absence of swelling effects (Eq. S19a) and E^*_{cr} represents the amended dry state expectation for a given sample-fluid couple with $\mathcal{S}_r > 1$. We also note that in above we have neglected the swelling (expansion) of h and s_κ because the top of the pillars are not wetted by the fluid and the base substrate is thick relative to the pillar height. Accounting for such, results in $E^*_{\text{cr}} \propto \mathcal{S}_r^3$ (as opposed to $E^*_{\text{cr}} \propto \mathcal{S}_r^2$ expressed in Eq. S19b). Nevertheless, we use $E^*_{\text{cr}} \propto \mathcal{S}_r^2$ because this scaling matches well with our experimental findings (Fig. 6 [manuscript] and Sec. S12C below).

S12C: Considering the pillar clustering results for Eco25 during evaporative drying (Fig. 6 [manuscript], Movie S2), Eq. S19a yields respective values of $E_{\text{cr}} \sim 125$, ~ 120, and ~ 105 kPa (or $\frac{E_{\text{cr}}}{E_0} \approx 0.89$, 0.86, and 0.75) for Eco25-EtOH, Eco25-IPA, and Eco25-IsoO; relative to $E_0 = 140 \pm 50$ kPa measured for Eco25 (Sec. S5, Tables S2 and S4). While these calculated E_{cr} values are within $10 \sim 25$ % of E measured for Eco25, the $E_{\text{cr}}/E_0 \geq 1$ clustering criteria is not quite reached. Moreover, counter to our experimental observations, Eq. S19a predicts that Eco25 pillar clustering is most likely with the EtOH working fluid $(\frac{E_{\text{cr}}}{E_0}|_{\text{EtOH}} > \frac{E_{\text{cr}}}{E_0}|_{\text{IPA}} > \frac{E_{\text{cr}}}{E_0}|_{\text{IsoO}})$. On the other hand, accounting for swelling effects (Eq. S19b), the predicted E^*_{cr} threshold (or likelihood) for Eco25 pillar clustering increases to values of $E^*_{\text{cr}} \sim 135$, ~ 143, and ~ 192 kPa (or $\frac{E^*_{\text{cr}}}{E_0} \approx 0.96 \pm 0.26$, 1.02 ± 0.28, and 1.37 ± 0.42) for EtOH, IPA, and IsoO (respectively). Thus, now our proposed $E^*_{\text{cr}}/E_0 \gtrsim 1$ clustering criteria is satisfied for Eco25-EtOH, Eco25-IPA, and Eco25-IsoO (given the measured elastic heterogeneity of Eco25, $E_0 = 140 \pm 50$ kPa). Also, now our swelling-enhanced clustering predictions correlate with that experimentally observed – i.e. Eq. S19b predicts that Eco25 pillar clustering is most likely with the IsoO working fluid $(\frac{E^*_{\text{cr}}}{E_0}|_{\text{IsoO}} > \frac{E^*_{\text{cr}}}{E_0}|_{\text{IPA}} > \frac{E^*_{\text{cr}}}{E_0}|_{\text{EtOH}})$.

S12D: Eq. S19b can also be used to predict the critical dry state modulus for micropillar clustering during the hemiwicking process. For this transient analysis, the equilibrium $\mathcal{S}_r$ in Eq. S19b must be replaced with the temporally-scaled $\mathcal{S}^*_r$ (Eq. S32, Sec. S17) and θ_{Rec} should be replaced with θ_{Eq}. For Eco25, the

timescale for complete pillar wetting (micro-pumping) is $t^*_{\rm w} \approx 20 \pm 10$ ms (Fig. 5*A* [manuscript], Movie S2). Correspondingly, the transient swelling ratios for Eco25-EtOH, Eco25-IPA, and Eco25-IsoO in $t^* \approx 20$ ms are $\mathcal{S}^*_r \approx 1.004$, 1.008, and 1.074 (respectively); yielding transient, dry state critical modulus ratios of $E^*_{\rm cr}/E_0 \approx 0.63 \pm 0.21$, 0.73 ± 0.25, and 0.86 ± 0.29 for EtOH, IPA, and IsoO (respectively). Thus, given the elastic heterogeneity of Eco25 and transient swelling effects, Eco25 pillar clustering is only predicted under these representative hemiwicking conditions (and only observed) with the IsoO working fluid.

Concurrent expectations abide with the Eco50-IsoO couple (Movie S1) – i.e., the only other sample-fluid couple tested that exhibited pillar clustering during both hemiwicking and sample drying (evaporation). For example, in $\approx$20 ms of hemiwicking with Eco50-IsoO and PDMS(D6)-IsoO, we calculate $E^*_{\rm cr}/E_0 \approx 0.58$ and ≈ 0.07 (respectively). Thus, transient pillar clustering ($E^*_{\rm cr}/E_0 \geq 1$) is not expected with either Eco50-IsoO or PDMS(D6)-IsoO during the early stages of the hemiwicking process. This is exactly what is experimentally observed (Movie S2). We do note that the Eco50-IsoO (sample-fluid) couple did exhibit pillar clustering during hemiwicking; yet, only at extended wicking (or swelling) times ($t^* \approx 150 \pm 80$ ms, Movie S1). Given the elastic heterogeneity of Eco50 ($E_0 \approx 230 \pm 70$ kPa) and the increased swelling time interval ($t^* \approx 150 \pm 80$ ms), we have correspondingly $\mathcal{S}^*_r \approx 1.15 \pm 0.04$ (Sec. S18B); which subsequently yields for Eco50-IsoO during hemiwicking the predicted agreement of $E^*_{\rm cr}/E_0 \approx 0.78 \pm 0.38$.

S13: Meniscus interface diffusivity

After the hemiwicking flow becomes developed ($\ell \geq \ell_e$), the meniscus front propagates in time like a diffusion process (13, 25). The mean-squared displacement of the wicking front is

$$\ell^2 = 2nD_I t, \qquad \text{[S20]}$$

where D_I is the meniscus interface diffusivity, n is the dimension of the displacement, and t is the wicking time. Taking the time derivative of Eq. S20 and setting $n = 1$ of 1D diffusion, leads to $\ell \frac{d\ell}{dt} = D_I$. If Eq. S8 is substituted for the $\frac{d\ell}{dt}$ velocity in $\ell \frac{d\ell}{dt} = D_I$, then the following is predicted for the interface diffusivity:

$$D_I = \frac{1}{C_{d0}} \left(\frac{\gamma}{\mu} \right) K, \qquad \text{[S21]}$$

where $C_{d0} = 24$ and K is calculated with Eq. S9 (and supporting Eqs. S10a–S11c).

The correlation between D_I (measured) and that predicted by Eq. S21 is typically within a factor of 2 (i.e., $0.5 \lesssim \bar{D}_I/D^{\rm p}_I \lesssim 2$, Fig. 7*D* [manuscript]). As a related comment, we note that in past studies (13, 21) that the $2n$ in Eq. S20 was not included; in result, the previously predicted D_I equation for hemiwicking was a factor of 2 greater than that provided in Eq. S21. And consequently, the meniscus interface diffusivity analysis discussed in Refs. (13, 21) have tabulated and plotted D_I values that are a factor of 2 to large. The raw (ℓ^2 vs. t) hemiwicking data plotted in those studies are still correct; yet, the reported D_I values obtained from the fitted slope ($\frac{d}{dt}\ell^2$) were not divided by 2 (in accordance with Eq. S20 with $n = 1$). Future studies need to explore the broader impacts of Eq. S20–S21 with porous wicking media ($2 \leq n \leq 3$).

S14: Dissipation effects on the hemiwicking capillary pumping efficiency

The fluid-induced surface and pillar deformations are not entirely elastic (i.e., $E = E' + iE''$). We find that the dissipation in the capillary pumping efficiency (via inelastic sample surface or pillar deformations) can be rather significant for soft pillar arrays ($E \lesssim 150$ kPa) and fluids that induce appreciable swelling.

A reduction in the meniscus pumping power can be evaluated starting from

$$U_{\rm wick} = U_0 - U_{\rm loss}, \qquad \text{[S22]}$$

with a corresponding damped or reduced pumping efficiency,

$$\eta_{\rm wick} = \eta_0 \, \eta^*_{\rm pump} = \eta_0 \left(1 - \frac{U^*_{\rm loss}}{U_0} \right), \qquad \text{[S23]}$$

where η_0 represents the hemiwicking efficiency tied to the viscous drag losses (Eq. S5–S8), $U_0 \approx \gamma \cos\theta(2r_p h)$ is the corresponding capillary pumping energy per unit wicking cell without viscoelastic losses (abiding with Eq. S7), and U^*_{loss} represents the additional dissipative losses in the pumping energy (per unit wicking cell) not accounted for in our hemiwicking model (Eq. S5–S8).

Application of Eq. S22–S23 leads to the revised hemiwicking performance equation:

$$\tilde{D}_I \approx D_I \, \eta^*_{\text{pump}}, \tag{S24}$$

where the meniscus interface D_I diffusivity can be calculated with Eq. S21 (i.e., D_I from our hemiwicking model with $\eta_0 < 1$ already accounted for via the viscous drag losses with the pillar walls). In principle, D_I and $\tilde{D}_I$ in Eq. S24 can be replaced with $\text{v}(\ell)$ and $\tilde{\text{v}}(\ell)$ to account for any additional dissipation-induced reductions in the hemiwicking velocity (Fig. S9). In either case, the capillary pumping efficiency is reduced proportional to the relative amount of energy dissipated during each micro-pumping event in the hemiwicking process.

We note that multiple loss mechanisms can contribute to U_{loss}. For example, losses tied to inelastic pillar deflections, fluid-induced sample swelling, and elastocapillary surface deformations at the contact line. The losses due to viscous (Stokes) drag are not intended to be included in the U_{loss} term in Eq. S22 because they are already accounted for in η_0 (Eq. S23) via the hemiwicking model derivation (Eq. S5–S8). The following addresses our U_{loss} calculations for reductions in the hemiwicking performance due to inelastic pillar deflections (Sec. S15), elastocapillary deformations (Sec. S16), and transient swelling (Sec. S17).

S15: Effects of inelastic pillar deflections on the hemiwicking dynamics

If U_{loss} is only due to inelastic pillar deflections, then U_{loss} can be evaluated based on the inelastic reductions in the potential energy of the deflected pillar:

$$U^*_{\text{loss},\mathcal{B}} \approx \frac{1}{2} k'' \delta_p^2. \tag{S25}$$

Eq. S25 represents the pillar bending energy (Joules [J]) dissipated per unit wicking cell. Eq. S25 can be derived from first principle stress-strain analysis, where $u_{\mathcal{B}} = \frac{1}{2}\frac{B}{R^2_{\mathcal{B}}}$ is the bending energy per unit rod length [J/m], $B = \frac{\pi}{4} E\, r_p^4$ is the bending modulus of a cylindrical rod, and $R_{\mathcal{B}} \approx L^2/\delta_p$ is the bending radius of curvature of the rod. Neglecting the shear, torque, and pillar base contributions (26), the effective spring bending constant of a cylindrical (CYL) pillar of length ($L = h$) and radius (r_p) is then $k \approx \frac{\pi}{4} E\, r_p^4/h^3$. Therefore, $k'' \approx \frac{\pi}{4} E'' \bar{r}_p^4/h^3$ for inelastic CYL pillar deflections, where $E'' = E' \tan\varphi$, E' is the Young's modulus of the wicking array (Eq. S3), $\tan\varphi = E''/E'$ is the loss tangent (or dissipation factor). Herein we also assume that the pillars have the same dry state elastic modulus as that measured for the base substrate ($E'_p = E'_{\text{sub}} = E_0$).

We note that k'' (or E'') is used rather than k' in Eq. S25. For purely elastic bending, $k'' = 0$ and the energy transferred from the fluid to the pillar is restored back to the fluid during pillar recoil. Also, the pillar deflections are primarily in-line with the wicking front propagation direction (Movie S2). Moreover, if $k'' = 0$, then $\eta^*_{\text{pump},\mathcal{B}} \approx 1$ and the wicking performance returns to that already described by our hemiwicking model ($\eta_{\text{wick}} = \eta_0$). Of course this result is based on the expectation that elastic (or inelastic) pillar deflections do not induce additional viscous drag losses beyond that already accounted for in Eq. S6. In support of the latter, the hemiwicking flow is already in the Stokes flow regime and the transient pillar deflections ($\frac{d}{dt}\delta_p \lesssim \text{v}$) are also primarily parallel to the net flow direction (Movie S2). Hence, notable increases in C_d or A_{C_d} are not expected for elastic (or inelastic) pillar deflections.

The magnitude of δ_p in Eq. S25 can be both measured (Movie S2) and calculated (Eq. S17). Using Eq. S17 for δ_p with $z \approx h$, the inelastic losses per unit wicking cell due to transient pillar deflections are expected to scale as

$$U^*_{\text{loss},\mathcal{B}} \approx \frac{(\gamma \cos\theta)^2}{2\pi} \left(h^5/r_p^4\right) \left[\frac{\tan\varphi}{E'}\right]. \tag{S26}$$

The corresponding reduction in the hemiwicking pumping energy (Eq. S23) is then

$$\frac{U^*_{\text{loss},\mathcal{B}}}{U_0} \approx \frac{\gamma\cos\theta}{4\pi}\left(h^4/r_p^5\right)\left[\frac{\tan\varphi}{E'}\right], \qquad \text{[S27]}$$

where $U_0 \approx \gamma\cos\theta(2r_p h)$ is the potential capillary pumping energy per unit wicking cell (via Eq. S7).

S15A: We point out that $\frac{U^*_{\text{loss},\mathcal{B}}}{U_0}$ (Eq. S27) scales as $1/E'$, which abides with the $1/E$ dependence observed for hemiwicking with the PDMS and PDMS-Ecoflex composite samples (Fig. 7*D,E* [manuscript]). However, as we will address below, reductions in the pumping efficiency from solely inelastic pillar deflections are not enough to explain the soft wicking behavior observed herein.

S15B: Considering the upper-limit dissipation scenario for hemiwicking with transient pillar clustering (i.e., $\delta_p = s_\kappa$ during the onset of hemiwicking with Eco25-IsoO), the wicking performance is expected to be reduced by up to ∼7 %. For example, using the Eco25-IsoO sample-fluid properties (Table S4) and a corresponding $k'' = 7.7 \pm 4.8$ mN/m (or $E'' = 35.8 \pm 22.6$ kPa), Eq. S25 yields $\eta^*_{\text{pump},\mathcal{B}} \approx 96 \pm 3\%$ for the reduced pumping efficiency (Eq. S23) or $\tilde{D}_I/D_I \approx 0.96 \pm 0.03$ (Eq. S24). These k'' (or E'') values are based on a loss tangent of $\tan\varphi \approx 0.25 \pm 0.15$; obtained from complex modulus studies of PDMS fabricated under various curing conditions (27).

S15C: Again we point out that for the soft Eco25 sample that transient pillar deflections occur on a time scale comparable to that for complete pillar wetting – i.e., $\frac{d}{dt}\delta_p \lesssim$ v (or $\tau_w \approx 5 \sim 25$ ms, Movies S1-S2). For Eco25-EtOH and Eco25-IPA, transient Eco25 pillar deflections are observed in the range of 5 μm $\lesssim \delta_p \lesssim$ 20 μm (Movie S2), yielding pumping efficiency reductions on the order of $\eta^*_{\text{pump},\mathcal{B}} \gtrsim 98\%$ such that the $\lesssim 2\%$ inelastic bending losses are not expected to dampen the wicking performance. On the other hand, if the pillar deflections by the different fluids are on the order of the pillar height ($\delta_p \propto h - \bar{r}_p$), then $\eta^*_{\text{pump},\mathcal{B}} \approx 48 \pm 31\%$. Therefore, it is not surprising that the ultrasoft Eco0 sample did not hemiwick with IsoO and only partially hemiwicked with EtOH and IPA (Fig. 7*A–C* [manuscript]).

S15D: The preceding deflection analysis (and examples therewith) did not account for either (1) wicking energy losses tied to contact line surface deformations (transient elastocapillary effects) or (2) swelling-induced softening or stiffening of the pillars (28). Interestingly, the degree of swelling has recently been shown to be coupled to the magnitude of the surface deformations at the contact line (29). These additional effects of (1) contact line surface deformations and (2) sample swelling are addressed next in more detail (Sec. S16 and S17, respectively).

S16: Effects of contact-line surface deformations on the wicking and wetting dynamics

Several recent studies have addressed the length-scale of soft surface deformations by a fluid with an appreciable surface tension (25, 30–35). Such surface deformations at the solid-liquid-vapor contact line scale with the elastocapillary length for surface shear (34): $\Delta z \approx l_{\text{ec}}$, where $l_{\text{ec}} = \gamma/G$ is the elastrocapillary length, G is the shear modulus of the sample substrate, and γ is the surface tension of the fluid.

For an isotropic material, the shear modulus is $G = E/2(1+\nu)$, where ν is Poisson's ratio and E is Young's modulus. For Ecoflex, PDMS, and NOA61, Poisson's ratio is $\nu = 0.46 \pm 0.03$, 0.47 ± 0.02, and 0.34 ± 0.05, respectively (36). Aside from NOA61, the shear modulus of the softer materials studied scale as $G \approx \frac{1}{3}E$. Therefore, submicron surface deformations (normal to the hemiwicking flow-field direction) are expected for all sample-fluid combinations studied herein. For example, for Eco0-Iso0, $l_{\text{ec}} = 0.92 \pm 0.17$ μm, whereas for the stiffer samples studied ($E \geq 140$ kPa), $l_{\text{ec}} < 0.5$ μm.

Elastocapillary surface (or wetting ridge) deformations on the order of $l_{\text{ec}} \lesssim 1$ μm seem rather insignificant. However, during a dynamic wicking or wetting process, these nanoscale-to-micronscale surface deformations turn out to be rather important – especially for ultrasoft materials and soft sample-fluid combinations with enhanced swelling effects.

The energy dissipated during this contact line motion over the wall surface is effectively that of a volumetric strain (i.e., a bulk pillar strain due to a propagating strain wave or surface wrinkle of amplitude

$\Delta z \propto l_{\rm ec}$). The corresponding pumping energy loss (per unit wicking cell) is estimated from the isotropic strain energy density:

$$U_{\mathcal{E}} = \frac{1}{2}\int E\,\epsilon_{\mathcal{E}}^2\,dV. \qquad \text{[S28]}$$

where $\epsilon_{\mathcal{E}}$ represents the elastocapillary induced strain over the deformed pillar surface region of initial volume V_{p_0}. During hemiwicking, the top and base pillars are not wetted by the fluid; so, the effective strain is tied to an effective propagating biaxial strain ($\Delta V/V \approx 2\,\epsilon_{\mathcal{E}}$) on the pillar walls as the walls are wetted by the propagating meniscus (triple-line). The resulting *viscoelastic* energy dissipated for this propagating elastocapillary wetting ridge deformation (per unit wicking cell) should scale as

$$U^*_{\text{loss},\mathcal{E}} \approx \frac{1}{2}V_{p_0}E'\,\epsilon_{\mathcal{E}}^2, \qquad \text{[S29a]}$$

$$U^*_{\text{loss},\mathcal{E}} \approx \frac{1}{2}V_{p_0}E'\,[2l_{\rm ec}/r_p]^2\,, \qquad \text{[S29b]}$$

$$U^*_{\text{loss},\mathcal{E}} \approx \frac{1}{2}V_{p_0}E'\,[4\gamma(1+\nu)/E'r_p]^2\,. \qquad \text{[S29c]}$$

For S29a→S29b, we have used the equivalent strain (or logarithmic strain) induced by the propagating wetting ridge in the low strain limit (e.g., $\bar{\epsilon}_{\mathcal{E}} = \ln\frac{A}{A_0} \to \ln\frac{\pi r^2}{\pi r_0^2} \to 2\ln\frac{r}{r_0} \to 2l_{\rm ec}/r_p$). Then, for S29b→S29c, $l_{\rm ec}$ is expressed in terms of the Young's modulus, yielding the expected $1/E'$ dependence to the dissipative losses by transient elastocapillary effects. Also, now swelling-induced softening (28) of the micropillars is expected to enhance these dissipation effects. With respect to Eq. S23, the corresponding reduction in the pumping efficiency due to a propagating elastocapillary wetting ridge deformation is

$$\frac{U^*_{\text{loss},\mathcal{E}}}{U_0} \approx \frac{4\pi}{r_p}\frac{\gamma(1+\nu)^2}{E'\cos\theta}\,\phi_{A_{\mathcal{E}}}\,, \qquad \text{[S30]}$$

where $V_{p_0} = \pi r_p^2 h$ and $U_0 \approx \gamma\cos\theta(2r_p h)$ is the capillary pumping energy per unit wicking cell.

S16A: We note that Eq. S29a→S29c only account for the dissipative losses during the wetting of the pillar wall surfaces. To account for the extra dissipation from the base wall surface of the wicking array, Eq. S30 has been multiplied by the surface area ratio $\phi_{A_{\mathcal{E}}} = A_t/A_p$, where A_p is wetted pillar wall surface area, A_t is the total wetted surface area (per unit wicking cell), and $\phi_{A_{\mathcal{E}}} \approx 1.3$ for the PDMS (D1−D6) and Ecoflex (Eco0−to−Eco50) wicking samples.

S16B: Based on this scaling analysis (Eq. S30), the elastocapillary energy losses with the soft Eco25 wicking array are *quite significant* – e.g., $\frac{U^*_{\text{loss},\mathcal{E}}}{U_0} \approx 26.8\,\%$, $23.2\,\%$, and $17.2\,\%$ for EtOH, IPA, and IsoO (respectively). Moreover, if wicking samples are softer than 30 kPa (or the wicking arrays are of very slender pillars, $r_p \lesssim 10\ \mu$m), then $\frac{U^*_{\text{loss},\mathcal{E}}}{U_0} \gtrsim 80\,\%$ (see also the predicted $U^*_{\text{loss},\mathcal{E}}$ contributions in Fig. S8). However, both of these latter conditions are not suitable for sustainable, 2D soft matter hemiwicking arrays – closely matching what we experimentally observe with wicking arrays made from Ecoflex – i.e., ultrasoft, slender pillars want to rapidly fold and cluster after fluid meniscus exposure.

S16C: While it seems plausible that propagating elastocapillary surface deformations can induce a notable dissipation in the capillary pumping energy (Eq. S30), more detailed investigations are still needed – especially because of the allusive and rapid coupling between swelling and the elastocapillary wetting observed with the ultrasoft Ecoflex [$\sim$61 kPa] Eco0 sample (Fig. S2 and Fig. 1 [manuscript]).

S17: Effects of sample swelling on the wicking and wetting dynamics

The kinetics and thermodynamics of sample swelling has a long, interesting history; pioneered by the early work of Paul. J. Flory (22–24) and now addressed in several unique studies by various researchers (25, 28, 29, 37–41). Abiding with the analysis in Ref. (37), the swelling energy can be estimated from the strain energy density as

$$U_{\mathcal{S}} = \frac{1}{2}V_{p_0}E\,\epsilon_{\mathcal{S}}^2 \approx \frac{1}{2}V_{p_0}E\,(\mathcal{S}_r - 1)^2, \qquad \text{[S31]}$$

where $\epsilon_{\mathcal{S}} \approx (\mathcal{S}_r - 1)$ is used to couple the swelling strain per unit wicking cell to the equilibrium $\mathcal{S}_r$ swelling ratio. The magnitude of $\mathcal{S}_r$ is dependent on both the sample material and the type of fluid (solvent). For an isotropic material in a given solvent, the volume swelling ratio is $V/V_0 = \mathcal{S}_r^3$.

S17A: Eq. S31 estimates the total swelling energy during the transition from the initial *dry equilibrium* state to the final *swelled equilibrium* state. However, the final swelled equilibrium state is reached at a time scale much greater than the time scale for pillar wetting (e.g., full equilibrium swelling of a micropillar in the wicking array is expected in $t_{\mathcal{S}} \gtrsim 2 \sim 30$ seconds, whereas the sidewalls of pillars are fully wetted typically within $5 \sim 50$ ms (Fig. 5–7 [manuscript], Sec. S18, Movies S1, S2). Therefore, the actual pumping power dissipated via swelling should only be a fraction of that predicted by Eq. S31. Moreover, it is not clear if swelling induces a net dissipation in the pumping power. For example, after the pillars are fully wetted, the diffusive swelling in the hemiwicking array potentially augments the hemiwicking flow.

S17B: For a conservative estimate of the losses during capillary pumping, (1) E in Eq. S31 is replaced by the loss modulus, E'', and (2) the swelling ratio contribution in Eq. S31 is temporally weighted based on the self-similar solution for the short time swelling kinetics (39–41). In regards to the latter, the temporally weighted swelling ratio to be applied to Eq. S31 is

$$\mathcal{S}_r^*(t^*) = 1 + 2(\mathcal{S}_r - 1)\sqrt{t^*/\pi\tau_{\mathcal{S}}}, \qquad \text{[S32]}$$

where $\mathcal{S}_r$ is the equilibrium swelling ratio, $\tau_{\mathcal{S}} \approx r_p^2/D_{\mathcal{S}}$, and $D_{\mathcal{S}}$ is the intrinsic solvent swelling diffusivity.

Based on Eq. S32 for $t^* \ll \tau_{\mathcal{S}}$, the pillars radially expand during hemiwicking as $r_p(t^*) = r_p\,\mathcal{S}_r^*(t^*)$. Herein, we neglect swelling-induced changes the pillar height because the top and bottom of the pillars are not wetted. These assumptions may breakdown for $t^* \gg t_{\mathrm{w}}^*$; certainly if instantaneous swelling mechanisms exist (39, 41). Furthermore, in terms of this dynamic wetting of the pillar walls during each micro-pillar pumping/wetting process, we apply a spatially-averaged degree of swelling: $\bar{r}_p(t_{\mathrm{w}}^*) = [r_p(t_{\mathrm{w}}^*) + r_p]/2$ – or, in terms of an averaged swelling ratio, $\bar{\mathcal{S}}_r^* \approx \frac{1}{2}[\mathcal{S}_r^*(t_{\mathrm{w}}^*) + 1]$. Application of Eq. S32 also requires knowledge of $\tau_{\mathcal{S}}$ (or $D_{\mathcal{S}}$). We have found that the equilibrium swelling time can be approximated fairly well using $\tau_{\mathcal{S}} \sim \frac{L_c^2}{D_{\mathrm{SE}}}(\frac{\mathcal{S}_r^3}{\mathcal{S}_r^3-1})$; yet, this scaling does not account for the stiffness dependence to $\mathcal{S}_r(t)$ (Eq. S43, Sec. S18).

S17C: Below addresses our approach for evaluating $\tau_{\mathcal{S}}$ in terms of (1) the initial, dry state elastic properties (E', E'', ν) of the wicking sample and (2) the corresponding changes in the osmotic pressure of a given sample-fluid couple during swelling. Neglecting any swelling effects after the pillars are fully wetted ($t > t_{\mathrm{w}}^*$), replacing E' with E'' in Eq. S31, along with using Eq. S32 for the average swelling in t_{w}^* time, we have the following relations for the swelling energy dissipated per unit wicking cell:

$$U_{\mathrm{loss},\mathcal{S}}^* \approx V_{p_0} E'' \,(\mathcal{S}_r - 1)^2 \left[\frac{t_{\mathrm{w}}^* D_{\mathcal{S}}}{\pi r_p^2}\right], \qquad \text{[S33a]}$$

$$U_{\mathrm{loss},\mathcal{S}}^* \approx V_{p_0} E'' \,(\mathcal{S}_r - 1)^2 \left[\frac{t_{\mathrm{w}}^* D^m}{\pi r_p^2}\right] \frac{k_B T}{\Omega_s E'}\,\xi(\nu), \qquad \text{[S33b]}$$

$$U_{\mathrm{loss},\mathcal{S}}^* \approx \frac{V_{p_0}}{\Omega_s}\left[\frac{E''}{E'}\right](\mathcal{S}_r - 1)^2 \left[\frac{t_{\mathrm{w}}^* D_{\mathrm{SE}}}{\pi r_p^2}\right] k_B T\,\xi(\nu)\,\Pi_{0'}(\mathcal{S}_{\bar{r}}), \qquad \text{[S33c]}$$

$$U_{\mathrm{loss},\mathcal{S}}^* \approx \frac{V_{p_0}}{\Omega_s}\,\tan\varphi\,(\mathcal{S}_r - 1)^2 \left[\frac{t_{\mathrm{w}}^* D_{\mathrm{SE}}}{\pi r_p^2}\right] k_B T\,\xi(\nu)\,\Pi_{0'}(\mathcal{S}_{\bar{r}}). \qquad \text{[S33d]}$$

For Eq. S33a–S33c, we have first coupled $D_{\mathcal{S}}$ to the mutual-diffusion D^m coefficient – similar to that done in Ref. (39) with the cooperative-diffusion coefficient, where $\Omega_s = V_{\mathrm{m}}/N_A$ is volume per solvent molecule and the function $\xi(\nu) = (1 - 2\nu)$ is for unconstrained swelling (39). Then, D^m is evaluated from its dependence to changes in the osmotic Π pressure: $D^m \approx \frac{1}{f^0}\frac{\partial\Pi(\rho_c)}{\partial\rho_c}$ (see, Eq. 1 in Ref. (42)), where $f^0 = k_B T/D_{\mathrm{SE}}$ is a constant mutual-friction coefficient. For reference, for free, isotropic swelling the osmotic pressure is $\Pi = \rho_c k_B T(1/\mathcal{S}_r - 1/\mathcal{S}_r^3)$, where $G' = \rho_c k_B T$ is the dry state shear modulus and

ρ_c is the effective number of polymer chains per unit volume in the dry state (43). We consider herein $\Pi = \rho_c k_B T(1 - 1/\mathcal{S}_r^2)$ for the osmotic pressure of a thin, swelling polymer rod (43). This leads to

$$D_{\mathcal{S}} \approx D^m \frac{k_B T}{\Omega_s E'} \xi(\nu) \approx D_{\mathrm{SE}} \frac{k_B T}{\Omega_s E'} \xi(\nu)\, \Pi_{0'}(\mathcal{S}_{\bar{r}}), \qquad [S34]$$

where $D^m \approx D_{\mathrm{SE}} \frac{\partial(\Pi/k_B T)}{\partial \rho_c}$ and $D_{\mathrm{SE}} = k_B T/(6\pi\mu\Omega_s^{1/3})$ is the used Stokes-Einstein relation for self diffusion.

In regards to the $\Pi_{0'}(\mathcal{S}_{\bar{r}})$ contribution in Eq. S33c–S34, we have used $\mathcal{S}_{\bar{r}} = \frac{1}{2}[\mathcal{S}_r + 1]$ rather than the equilibrium $\mathcal{S}_r$ to account for the short time swelling kinetics ($t_{\mathrm{w}}^* \ll \tau_{\mathcal{S}}$). We have also neglected the instantaneous surface swelling kinetics addressed by Huang et al. (39, 41) because our experimental results do not clearly reveal such effects. Perhaps such instantaneous swelling effects are better tied to the rapid elastocapillary surface deformations discussed in Sec. S16. In either case, the intrinsic solvent swelling diffusivity (Eq. S34) now scales as expected for both soft-to-rigid materials and sample-fluid couples with negligible swelling – e.g., for both free and constrained swelling: $D_{\mathcal{S}} \to 0$ as $E' \to \infty$ and $D_{\mathcal{S}} \to 0$ as $\mathcal{S}_r \to 1$. In Eq. S34, $\Pi_{0'}(\mathcal{S}_{\bar{r}})$ is used for shorthand, where $\frac{\partial \Pi(\rho_c)}{\partial \rho_c} \approx k_B T(1 - 1/\mathcal{S}_{\bar{r}}^2)$, $\frac{\partial(\Pi/k_B T)}{\partial \rho_c} \approx \Pi_{0'}(\mathcal{S}_{\bar{r}})$, and $\Pi_{0'}(\mathcal{S}_{\bar{r}}) = (1 - 1/\mathcal{S}_{\bar{r}}^2)$ for the anisotropic swelling of a polymer rod.

S17D: Eq. S33d provides the expected swelling energy dissipated per unit wicking cell, where E''/E' (in Eq. S33c) has been replaced with $\tan\varphi$. In this case, if $\tan\varphi$ is a constant, then the reductions in the pumping efficiency appear to be independent of the sample stiffness. This would be certainly predicted for $U^*_{\mathrm{loss},\mathcal{S}}$ if E' (in Eq. S33a) was used rather than E''. Nevertheless, $\tan\varphi$ is not a constant and is dependent on the magnitude of E' (i.e., $\frac{\partial \tan\varphi}{\partial \ln E'} \neq 0$). In fact, for the PDMS samples studied by Rubino and Ioppolo (27), we find via data analysis of their results that $\frac{\partial \tan\varphi}{\partial \ln E'} \approx -0.11 \pm 0.03$ with $\tan\varphi \approx 0.25$ at $E' \approx 1$ MPa in the low-frequency limit. Moreover, for the polymer composites studied by Weder et al. (44), we have also found a similar sensitivity of $\frac{\partial \tan\varphi}{\partial \ln E'} \approx -0.11 \pm 0.01$ with $\tan\varphi \approx 0.3$ at $E' \approx 1$ GPa near room temperature. Therefore, rather than using a constant value for $\tan\varphi$, the E' dependence to $\tan\varphi$ in Eq. S33d is scaled in terms of a power law that abides with the PDMS loss tangent results in (27) – e.g., $\tan\varphi = \tan\acute{\varphi}\,(E_\star/E')^{1/3}$ with $\tan\acute{\varphi} = 0.25$ and $E_\star = 1$ MPa. In result, we now have

$$\frac{U^*_{\mathrm{loss},\mathcal{S}}}{U_0} \approx \frac{\pi r_p\, k_B T}{2\Omega_s \gamma \cos\theta} \tan\acute{\varphi} \left[\frac{E_\star}{E'}\right]^{\frac{1}{3}} (\mathcal{S}_r - 1)^2 \left[\frac{t_{\mathrm{w}}^* D_{\mathrm{SE}}}{\pi r_p^2}\right] \xi(\nu)\, \Pi_{0'}(\mathcal{S}_{\bar{r}}). \qquad [S35]$$

for the expected swelling-induced reduction in the hemiwicking pumping efficiency per unit wicking cell.

S17E: PDMS swelling ratios with several different solvents have been measured by Whitesides et al. (45). Maximal swelling is expected when $(\partial_{\mathrm{t}}^{\mathrm{s}} - \partial_{\mathrm{t}}^{\mathrm{f}})^2 \to 0$, where $\partial_{\mathrm{t}}^{\mathrm{s}}$ and $\partial_{\mathrm{t}}^{\mathrm{s}}$ are the solubility parameters of the solid and fluid (Tables S1 and S2). Based on the equilibrium $\mathcal{S}_r$ results listed in Ref. (45) and related published values for $\partial_{\mathrm{t}}^{\mathrm{Eco0}}$, $\partial_{\mathrm{t}}^{\mathrm{PDMS}}$, and $\partial_{\mathrm{t}}^{\mathrm{f}}$ of the different fluids (f) studied herein, we use $\mathcal{S}_r \approx 1.04$, 1.09, and 1.35 for EtOH, IPA, and IsoO with Eco25 (respectively).

In support of $\mathcal{S}_r \approx 1.35$ for the Eco25-IsoO couple and the temporal scaling of $\mathcal{S}_r$ (Eq. S32–S34), the transient swelling of the wicking array was measured during the onset of hemiwicking with the Eco25-IsoO couple. For example, via analysis of the 1st pillar row in Movie S2, the s_y pillar spacing increased from ~ 130 μm to ~ 137 μm in $t^* = 21$ ms of IsoO wicking, which yields a respective $\mathcal{S}_r^* \approx 1.054$ in comparison to $\mathcal{S}_r^* \approx 1.057$ calculated with Eq. S32, using $\tau_{\mathcal{S}} \approx s_y^2/D_{\mathcal{S}}$, $D_{\mathcal{S}}$ calculated via Eq. S34, and the corresponding Eco25-IsoO (sample-fluid) properties (Tables S1, S2, and S4). In further support, the expected and measured swelling was $\mathcal{S}_r^* \lesssim 1.007$ for both Eco25-EtOH and Eco25-IPA in $t^* = 21$ ms of hemiwicking.

S17F: The expected reduction in the pumping efficiency can now be evaluated in terms of the $U^*_{\mathrm{loss},\mathcal{S}}/U_0$ ratio (Eq. S35). For example, using $\mathcal{S}_r \approx 1.04$, 1.09, and 1.35, $E' = E_0 \approx 140$ kPa, $E_\star = 1$ MPa, $\tan\acute{\varphi} = 0.25$, and a respective pillar wetting time of $t_{\mathrm{w}}^* = 20$ ms, the expected swelling energy loss ratios for Eco25 are $\frac{U^*_{\mathrm{loss},\mathcal{S}}}{U_0} \approx 0.1\%$, $\approx 0.3\%$, and $\approx 20.8\%$ for EtOH, IPA, and IsoO, respectively. Fig. S8 plots these swelling loss predictions with comparisons to D_I measured (see, Sec. S18).

S18: Characteristic timescales

The timescales for droplet dynamics are typically categorized by

$$\tau_\rho = \sqrt{\frac{\rho R^3}{\gamma}} \quad \text{(inertial or inertiocapillary)} \tag{S36}$$

$$\tau_\mu = \frac{\mu R}{\gamma} \quad \text{(viscous)} \tag{S37}$$

$$\tau_{\rm vc} = \frac{\mu^3}{\rho\gamma^2} \quad \text{(viscocapillary)} \tag{S38}$$

where for the fluids studied herein $\tau_\rho \gg \tau_\mu \ggg \tau_{\rm vc}$. τ_ρ is the conventional temporal scaling for the droplet wetting (Eq. S1). τ_μ is important when the capillary forces driving the wetting are damped by viscous dissipation (5). Sometimes τ_μ is referred to as the viscocapillary timescale; therefore, $\tau_{\rm vc}$ (for capillary wave dispersion at $\mathrm{v_{Ca}} = \gamma/\mu$) is also listed above.

For the rapid (upper-limit) wetting and wicking dynamics, both τ_ρ and $\mathrm{v_{Ca}}$ were shown to be quite important (respectively and collectively). The timescales for pillar micro-pumping (or pillar wetting) are

$$\tau_{\rm w}^{\rm on} \approx \frac{h}{\hat{\rm v}_{\rm wick}} \approx \frac{2C_{d0}h}{\hat{\rm v}_{\rm wet}} \quad \text{(onset of hemiwicking flow)} \tag{S39}$$

$$\tau_{\rm w}^{\rm d} \approx \frac{h}{\hat{\rm v}_{\rm wick}}\left(\frac{\ell}{\ell_e}\right) \quad \text{(developed hemiwicking flow)} \tag{S40}$$

where $C_{d0} = 24$ is Stokes drag coefficient, $\hat{\rm v}_{\rm wick} \approx \hat{\rm v}_{\rm wet}/2C_{d0}$ (Fig. 5*E* [manuscript], Eq. S12), $\hat{\rm v}_{\rm wet} \sim 1.5$ m/s (Eq. S2a), and the entrance lengths for the different wicking arrays and fluids studied herein are within $\ell_e \approx 0.3 \sim 2$ mm (Fig. 4*D*–*F* [manuscript], Sec. S10). For the sample-fluid combinations studied herein, $\tau_{\rm w}^{\rm on}$ ranges within $2 \sim 20$ ms. With comparisons to the droplet wetting timescales, we have $\tau_{\rm w} \sim \tau_\rho \gg \tau_\mu$.

The timescales for the different pillar deformation mechanisms discussed are

$$\tau_{\mathcal{E}} = \frac{l_{\rm ec}}{\mathrm{c_T}} \approx \frac{|\gamma|/G}{\sqrt{G/\rho_{\rm s}}} = \sqrt{\frac{\rho_{\rm s}\gamma^2}{G^3}} \quad \text{(elastocapillary)} \tag{S41}$$

$$\tau_{\mathcal{B}} \approx \frac{l_{\rm bc}}{\hat{\rm v}_{\rm wick}} \approx \frac{(B/\gamma)^{1/3}}{\hat{\rm v}_{\rm wick}} \quad \text{(pillar bending)} \tag{S42}$$

$$\tau_{\mathcal{S}} = \frac{L_c^2}{D_{\rm S}} \approx \frac{r_p^2}{D_{\rm SE}}\left(\frac{\mathcal{S}_r^3}{\mathcal{S}_r^3 - 1}\right). \quad \text{(swelling)} \tag{S43}$$

The elastocapillary timescale ($\tau_{\mathcal{E}}$, Eq. S41) is based on the magnitude of $l_{\rm ec}$ relative to the transverse speed of sound ($c_T = \sqrt{\rho_{\rm s}/G}$) with $\rho_{\rm s}$ being the bulk density of the wetted surface material (46). For the different fluids and PDMS-Ecoflex sample combinations studied herein, the elastocapillary deformations are very rapid relative to the that for pillar wetting (e.g., 1 ns $\lesssim \tau_{\mathcal{E}} \lesssim$ 250 ns, where 5 ms $\lesssim \tau_{\rm w} \lesssim$ 50 ms).

The pillar deflection timescale ($\tau_{\mathcal{B}}$, Eq. S42) is based on the bendocapillary $l_{\rm bc}$ length for cylindrical rod relative to the pillar wetting velocity. For reference, $B = \frac{\pi}{4} E\, r_p^4$ for a CYL pillar, whereas for a thin sheet of thickness t_s the bending modulus (per unit sheet width) is $B = \frac{Et_s^3}{12(1-\nu^2)}$ and $l_{\rm bc} = \sqrt{B/\gamma}$ (46). Similar to the deformation of soft sheets, significant bending of the micropillars are expected when $l_{\rm bc}/h < 1$. For the different fluids and PDMS-Ecoflex sample combinations studied herein, we have ratios spanning from $l_{\rm bc}/h \sim 0.8$ (Eco0-EtOH) to ~ 2.9 (PDMS(D6)-IsoO). Also, the observed pillar deflection timescales (Movie S2, Fig. 5*A* [manuscript]) are similar to that calculated for both $\tau_{\mathcal{B}}$ and $\tau_{\rm w}$. Therefore, it is not surprising that transient pillar clustering is observed with soft ($E < 150$ kPa) micro-pillar arrays.

The timescale for full equilibrium swelling ($\tau_{\mathcal{S}}$, Eq. S43) is much greater than the timescales for capillary pumping/wetting ($\tau_{\rm w}$), transient micro-pillar deflections ($\tau_{\mathcal{B}}$), and especially for elastocapillary deformations

($\tau_{\mathcal{E}}$) – i.e., $\tau_{\mathcal{S}} \gg \tau_{\rm w} \sim \tau_{\mathcal{B}} \ggg \tau_{\mathcal{E}}$. Eq. S43 is our approximation for $\tau_{\mathcal{S}}$ based on the self-similar solution for the swelling kinetics (39–41), where L_c is the characteristic length of the sample, $\mathcal{S}_r^3 = V/V_0$ is the equilibrium volume swelling ratio, and $D_{\rm SE}$ is the Stokes-Einstein solvent self-diffusion coefficient (see, Eq. S32, Eq. S34, and corresponding discussion in Sec. S17). For the Eco25 sample, this scaling with $L_c = r_p$ yields $\tau_{\mathcal{S}} \approx 14.5$, 14.7, and 1.7 seconds for the different EtOH, IPA, and IsoO fluids (respectively), matching quite well with that observed (Fig. 6 [manuscript]). We note that these estimates for $\tau_{\mathcal{S}}$ are based on $r_p = 26.7$ μm for Eco25, using $\mathcal{S}_r \approx 1.04$, 1.09, and 1.35 and $D_{\rm SE} \approx 4.42\times10^{-10}$, 2.13×10^{-10}, and 7.03×10^{-10} m^2/s calculated for Eco25-EtOH, -IPA, and -IsoO (respectively). While $\tau_{\mathcal{S}} \gg \tau_{\rm w}$, appreciable swelling is still observed during the early stages of the transient hemiwicking process (especially with the Eco25-IsoO (sample-fluid) couple; Movie S1 and S2). The timescale for transient pillar swelling can also be estimated using Eq. S43 with $L_c = \Delta r_p$; yet, Eq. S32 is recommended for predicting the short-time swelling kinetics.

S19: Swelling-induced softening

For the following discussion on swelling enhanced viscoelastic dissipation, we first must revisit the pioneering work of Paul J. Flory (22–24). As discussed in some of his early work, the elastic (stress-strain) properties of a cross-linked polymer (or rubber) are dependent of both the degree of deformation and the degree of swelling. In fact, he predicted that the modulus of elasticity (or tension at a given elongation) in a given solvent is inversely proportional to the five-thirds power of the swelling volume ratio – e.g.,

$$E(\epsilon, \mathcal{S}_r) \sim E_0 \mathrm{f}(\epsilon)/\mathcal{S}_r^5, \qquad \text{[S44]}$$

where E_0 represents the dry state elastic modulus ($E_0 \cong E'$) and f(ϵ) represents a function for the type of strain deformation. For the dissipation analysis addressed herein, the key points are that (1) the modulus of elasticity decreases as the polymer swells and (2) a tensile deformation, at an equilibrium or intermediate swelling state, produces an increase in the swelled modulus of elasticity.

S18A: This intrinsic stress-strain-swelling behavior (Eq. S44) predicted by Flory could result in some interesting nonlinearities in the swelling kinetics (e.g., $\mathcal{S}_r(t) \circlearrowleft D_{\mathcal{S}}(t)$). Yet, such effects on $U^*_{\text{loss},\mathcal{S}}/U_0$ should be small in the short time limit. Similarly, $U^*_{\text{loss},\mathcal{E}}/U_0$ predicted by Eq. S30 is also expected to have minor swelling-induced softening enhancements because $\tau_{\mathcal{E}} \ll \tau_{\rm w} \lll \tau_{\mathcal{S}}$ (Sec. S17). Yet, our inertial wetting data suggests otherwise (Fig. 1 [manuscript], Fig. S2). $U^*_{\text{loss},\mathcal{B}}/U_0$ predicted by Eq. S27, on the other hand, is clearly enhanced by rapid swelling (softening) of the micropillars (Fig. S8*B–D*, Sec. S12).

S18B: Sec. S12 briefly addressed the effects of swelling-induced softening in terms of the transient clustering of the Eco25 and Eco50 pillars during IsoO hemiwicking. Movie S2 demonstrates the rapid coupling between pillar bending, swelling, and clustering. For example, first the Eco25 micropillars are deflected by the propagating meniscus flow-field distribution ($t^* \lesssim 15$ ms); then, these bent pillars begin to increasingly swell with IsoO ($t^* \gtrsim t^*_{\rm w} \approx 20$ ms) with concurrent increases in δ_p until the onset of pillar clustering. Based on the combined use of Eq. S32, S34, and S44, we predict swelling-induced softening at timescales matching that observed for transient, threshold pillar clustering. For example, in only $t^* \approx 20$ ms of hemiwicking, we calculate swelling-induced softening for Eco25-IsoO on the order of $\approx$17%. Explicitly, $\frac{\Delta E(t^*)}{E_0} \propto 1-1/\bar{\mathcal{S}}^*_r(t^*)^5 \approx 1-1/1.037^5 \approx 17\%$, where $\bar{\mathcal{S}}^*_r(t^*) = \frac{1}{2}[\mathcal{S}^*_r(t^*)+1]$ is the spatiotemporally-averaged swelling in $t^* = 20$ ms (Eq. S32), using $\tau_{\mathcal{S}} = r_p^2/D_{\mathcal{S}}$, $D_{\mathcal{S}}$ (Eq. S34), and the corresponding sample-fluid properties (Tables S1-S4). For reference, the slightly stiffer ($\sim$230 kPa) Eco50 micropillars are expected to soften by $\frac{\Delta E(t^*)}{E_0} \approx 1-1/1.029^5 \approx 13\%$ in $t^* = 20$ ms, whereas $\frac{\Delta E(t^*)}{E_0} \approx 1-1/1.001^5 \lesssim 5\%$ is expected for the stiffest ($\sim$1980 kPa) PDMS (D6) micropillars during IsoO hemiwicking.

S20: Net energy dissipation effects on D_I and $\hat{\rm v}_{\rm wick}$

Figs. S8 and S9 overview our predicted effects of reductions in the pumping efficiency ($\eta^*_{\rm pump} = 1 - \frac{U^*_{\rm loss}}{U_0}$) on D_I and $\hat{\rm v}_{\rm wick}$ (respectively). This comparative analysis is limited to only the soft PDMS-Ecoflex hemiwicking samples because these samples were soft enough to exhibit transient pillar deformations, had

nearly identical wicking array geometries (r_p, h, s_x, s_y, α), and also had similar static and dynamic wetting properties (x_0, $\hat{\mathrm{v}}_{\mathrm{wet}}$, θ_{Eq}, θ_{Adv}, θ_{Rec}) for each respective working fluid.

Fig. S8*A* (or Fig. 7*E* [manuscript]) is a direct comparison between D_I measured (symbols) and that predicted (lines). The results are plotted as a function of the dry state Young's modulus of the wicking array. The symbol data come directly from linear regression fits of the measured mean-squared displacement of the hemiwicking front as a function of wicking time (Fig. 7*A*–*C* [manuscript]). The dashed horizontal lines are D_I^{p} predicted by Eq. S21 (i.e., that predicted for 1D hemiwicking flow with energy losses only due to viscous drag with the pillar walls). The solid line predictions correspond to $\tilde{D}_I = D_I^{\mathrm{p}} \times \eta_{\mathrm{pump}}^{*,\mathrm{net}}$ (Eq. S23–S24), where $\eta_{\mathrm{pump}}^{*,\mathrm{net}}$ accounts for the additional dissipative losses in the pumping energy due to (*i*) inelastic pillar defections ($U_{\mathrm{loss},\mathcal{B}}^*$, Eq. S27), (*ii*) propagating elastocapillary surface deformations ($U_{\mathrm{loss},\mathcal{E}}^*$, Eq. S30), and (*iii*) transient swelling ($U_{\mathrm{loss},\mathcal{S}}^*$, Eq. S35)). Figs. S8*B*–*D* show the predicted variations in η_{pump}^* in comparison to the $\bar{D}_I$ measured and then scaled as $\bar{D}_I/(D_I^{\mathrm{p}}\,\eta_0^*)$, where η_0^* serves as a normalization constant such that $\bar{D}_I^{\max}/(D_I^{\mathrm{p}}\,\eta_0^*) = 1$. The use of η_0^* as a normalization constant is not ideal. But, for some sample-fluid combinations $\bar{D}_I/D_I^{\mathrm{p}} > 1$ (Fig. 6*D* [manuscript]); therefore, we chose to use η_0^* for this comparative viscoelastic loss analysis.

Dissipative losses due to propagating elastocapillary surface deformations are not only the most practical, but are also predicted to be the most important (Fig. S8–S9). The best (poorest) agreement is found for the EtOH (IsoO) working fluid. Thus, better agreement is expected with IsoO if the swelling losses (Eq. S31) are based on measured $\mathcal{S}_r^*(t^*)$ and E'' values for each respective sample-fluid couple – rather than $\mathcal{S}_r^*(t^*)$ calculated with Eq. S32 and the use of a power law relationship for the loss tangent ($E''/E' \sim \tan\varphi\,(E_\star/E')^{1/3}$). Notable reductions in the hemiwicking performance are both observed and predicted when the dry state sample stiffness is less than $\sim$150 kPa. For example, for the soft ($E' \sim 140$ kPa) Eco25 hemiwicking sample, reductions of $\approx 35\,\%$, $\approx 43\,\%$, and $\approx 60\,\%$ were observed in comparison to the calculated reductions in the overall pumping efficiency on order of $U_{\mathrm{loss}}^{\mathrm{net}}/U_0 \approx 32\,\%$, $\approx 27\,\%$, and $\approx 45\,\%$ for EtOH, IPA, and IsoO working fluids (respectively). If $E' \lesssim 100$ kPa, then the predicted pumping efficiency rapidly approaches zero with increased (dry state) softening of the wicking array. The soft Eco0 sample turns out to have a dry state elastic modulus right around this transitional regime ($E_{\mathrm{c}} = 55$ kPa, Fig 7*D* [manuscript]). Moreover, the wicking velocities for Eco0 were significantly reduced at the onset of hemiwicking (e.g., < 0.5 mm/s with IsoO); so, the combination of pillar deflection, elastocapillary, and swelling energy losses seem reasonable for explaining the reduced wicking and wetting performances. With this said, our current analysis does not address the rapid ($t_{\mathrm{wet}}^* < 1 \sim 4$ ms) and drastically reduced ($\mathrm{v}(r^*)/\hat{\mathrm{v}}_{\mathrm{wet}} \lesssim 50\%$) droplet wetting dynamics observed with the IsoO working fluid (Fig. S2) - unless $\mathcal{S}_r$ is much greater in short exposure times than predicted by Eq. S32–S34. Certainly, this unique damped-to-recoil inertial wetting behavior observed with IsoO on ultrasoft surfaces needs further investigation, especially with sample substrates of varying thicknesses and other fluids with solubility parameters close to $\partial_{\mathrm{t}} \approx 13$ MPa$^{1/2}$ of Ecoflex (Eco0).

Supplementary Tables

Table S1. Fluid properties at 25°C and/or atmospheric pressure (1 atm).

Fluid	Density ρ (g/cm^3)	Surface tension γ (mN/m)	Viscosity μ (mPa·s)	Viscosity μ/ρ (mm^2/s)	Capillary velocity $\mathrm{v_{Ca}} = \gamma/\mu$ (m/s)	Solubility parameter $\partial_\mathrm{t} = \sqrt{\mathrm{c}}^*$ (MPa$^{1/2}$)	Heat capacity C_p (J/cm^3)	Latent Heat h_fg (kJ/kg)	Molar volume V_m (cm^3/mol)
Ethanol (EtOH)	0.789	21.83	1.074	1.361	20.3	26.4	1.941	839	58.367
Isopropanol (IPA)	0.786	21.55	2.038	2.593	10.4	23.5	2.107	749	76.547
Isooctane (IsoO)	0.690	18.60	0.478	0.693	38.9	14.2	1.465	307	165.1
Water	0.997	71.99	0.890	0.893	80.9	48.0	4.168	2257	18.015

$*$ – Hildebrand solubility parameter, $\partial_\mathrm{t} = \sqrt{\mathrm{c}} = (\partial_\mathrm{d}^2 + \partial_\mathrm{p}^2 + \partial_\mathrm{h}^2)^{1/2}$, where c is the cohesive energy density of the fluid and the subscripts d, p, and h represent the dispersion, polar, and hydrogen bonding contributions to ∂ (47, 48).

Table S2. Hemiwicking sample properties and replica molding conditions.

Sample Material	Code	Young's modulus E (MPa)	Poisson's ratio ν	Mixing ratios	Curing conditions t (hrs)	T (°C)	Density (g/cm^3)	Solubility parameter ∂_t (MPa$^{1/2}$)	$M_c^\ddagger$ (g/mol)
PDMS	D1	1.21±0.09	0.47±0.02*	10:1†	1	100	0.968	14.9-15.6	1496.6
PDMS	D2	1.16±0.09	0.47	10:1†	3	100	0.968	14.9-15.6	1561.1
PDMS	D3	0.39±0.13	0.47	15:1†	1	100	0.968	14.9-15.6	4643.3
PDMS	D4	1.95±0.19	0.47	10:1†	5	100	0.968	14.9-15.6	928.7
PDMS	D5	0.34±0.16	0.47	20:1†	1	100	0.968	14.9-15.6	5326.2
PDMS	D6	1.98±0.31	0.47	9:1†	5	100	0.968	14.9-15.6	914.6
Ecoflex	Eco0	0.061±0.009	0.46±0.03*	1:1$^{\mathrm{TM}}$	3	100	1.065	13*	32662
Eco/PDMS	Eco25	0.14±0.05	NA	75:25$^\mathcal{R}$, 1:1$^{\mathrm{TM}}$, 10:1†	3	100	1.037$^\phi$	13.6$^\phi$	13857
Eco/PDMS	Eco50	0.23±0.07	NA	50:50$^\mathcal{R}$, 1:1$^{\mathrm{TM}}$, 10:1†	3	100	1.014$^\phi$	14.1$^\phi$	8247.6
NOA61		175±61	0.34±0.05*	-	0.2$^{\mathrm{UV}}$	25	1.29	NA	13.79
JB-Weld		2070±450	NA	1:1	+24	25	1.92	NA	1.735

$\dagger$ – PDMS monomer-to-crosslink ratio (by mass). TM – Ecoflex$^{\mathrm{TM}}$ 00-30 [A:B] component ratio (by mass). $\star$ – Ref. (36) $*$ – Ref. (49)
$\ddagger$ – Calculated average molecular weight between crosslinks (50), using $E = \frac{4}{3}\rho RT/M_c$, $R = 8.3145$ J/K·mol, and $\rho_K \approx \frac{\rho N_A}{2M_c}$ [#/m^3].
ϕ – Calculated mass-averaged value. UV – UV light cured ($\lambda \sim$350 nm).
$\mathcal{R}$ – Ecoflex-to-PDMS mixing ratio (each uncured and by mass).

Table S3. Maximum wetting velocities, Young's modulus, and other key sample-fluid properties.

Sample Material	Code	Modulus E (MPa)	Max wetting speed, $\hat{\mathrm{v}}_\mathrm{wet}$ (m/s) EtOH	IPA	IsoO	Contact angle, θ_Eq (deg) EtOH	IPA	IsoO	Meniscus extension, x_0 (μm) EtOH	IPA	IsoO	Droplet radius, R (μm) EtOH	IPA	IsoO
PDMS	D1	1.21±0.09	1.50±0.29	1.45±0.39	1.60±0.35	45.5±4.3	31.4±3.6	$\leqslant$5	26.4±4.3	26.3±2.4	20.9±2.1	901±27	953±42	812±74
PDMS	D2	1.16±0.09	1.36±0.33	1.60±0.33	1.34±0.42	35.7±2.1	27.9±2.7	$\leqslant$5	27.2±3.1	25.6±3.3	27.9±2.8	864±46	937±21	846±86
PDMS	D3	0.39±0.13	1.45±0.39	1.49±0.29	1.33±0.37	40.4±3.6	31.3±4.3	$\leqslant$5	27.5±4.7	26.6±2.8	24.7±2.7	907±72	910±31	854±90
PDMS	D4	1.95±0.19	1.35±0.31	1.42±0.35	1.25±0.26	36.3±2.9	36.0±3.3	$\leqslant$5	20.5±4.3	20.6±3.1	27.6±3.3	947±62	943±14	869±54
PDMS	D5	0.34±0.16	1.45±0.33	1.55±0.35	1.45±0.31	41.1±2.6	35.8±3.2	$\leqslant$5	27.1±3.0	26.7±2.5	25.1±2.8	998±20	928±17	941±40
PDMS	D6	1.98±0.31	1.54±0.34	1.45±0.31	1.14±0.28	42.9±3.7	33.8±2.3	$\leqslant$5	26.7±3.7	25.1±2.4	30.2±3.9	913±99	889±50	887±29
Ecoflex	Eco0	0.06±0.01	–	0.91±0.25	0.50±0.08	29.3±2.5	27.0±1.5	$\leqslant$5	25.9±5.1	25.1±3.7	26.1±5.4	–	1534±35	1457±26
Eco/PDMS	Eco25	0.14±0.05	1.50±0.35	1.10±0.33	1.30±0.29	47.2±9.8	34.5±3.7	$\leqslant$5	27.4±4.3	26.5±2.7	26.2±5.3	868±35	860±61	889±21
Eco/PDMS	Eco50	0.23±0.07	1.35±0.31	1.43±0.29	1.45±0.32	49.7±3.6	29.2±3.5	$\leqslant$5	27.2±3.4	25.4±2.4	25.1±4.9	873±55	881±80	923±45
JB-Weld	R10	2070 ±450	–	–	–	15±5	$\leqslant$10	$\leqslant$5	24.1±6.9	22.0±7.1	27.3±5.7	–	–	–
JB-Weld	9U,M		0.91±0.39	1.10±0.35	1.37±0.42				74.3±21.9	72.2±15.6	51.5±15.3	828±83	835±90	780±78
NOA-61	9U,M	175±61*	1.11±0.41	0.87±0.31	1.32±0.40	15±5	$\leqslant$10	$\leqslant$5	51.7±13.1	60.1±19.5	55.6±14.9	830±85	833±87	785±82

$*$ - NOA-61 exhibited creeping sample restoration dynamics (e.g., 1-5 seconds for sample restoration after a moderate $\delta_{\hat{y}}$ >0.5 mm sample deflection).

Table S4. Hemiwicking samples, pillar geometries, and other key characteristic length-scales.

Table S4. Hemiwicking sample details, pillar geometries, and other key characteristic length-scales.

Sample		E	L	W	Pillar	height	base	slant	Wicking cell dimensions			R_h^{ocf}	$\bar{x_0}$ (μm)			K (μm)			$l_y^{1/4}$
Material	Code	(MPa)	(mm)	(mm)	shape	h (μm)	r_p (μm)	β (deg)	s_x (μm)	s_y (μm)	α (deg)	(μm)	EtOH	IPA	IsoO	EtOH	IPA	IsoO	(μm)
Ecoflex$^{\mathrm{TM}}$	Eco0	0.061	10	2.5	CYL	120.6	29.5	0	61.6	127.0	45.9	21.8	25.9	25.1	26.1	34.3	35.0	39.2	22.36
Eco/PDMS	Eco25	0.14	10	2.5	CYL	123.0	26.7	0	61.5	129.8	46.5	20.0	27.4	26.5	26.2	26.3	31.9	38.6	25.14
Eco/PDMS	Eco50	0.23	10	2.5	CYL	126.0	27.5	0	59.2	128.8	47.4	19.3	27.2	25.4	25.1	24.4	32.9	37.5	25.84
PDMS	D5	0.34	10	2.5	CYL	123.0	26.9	0	62.5	126.4	45.3	19.7	27.1	26.7	25.1	30.1	33.2	39.3	25.34
PDMS	D3	0.39	10	2.5	CYL	160.4	25.7	0	60.3	125.8	46.2	20.9	27.5	26.6	24.7	30.9	34.0	40.3	24.15
PDMS	D2	1.16	10	2.5	CYL	123.2	26.6	0	58.4	124.6	46.9	19.0	27.2	25.6	27.9	28.5	31.5	37.2	24.99
PDMS	D1	1.21	10	2.5	CYL	120.6	29.5	0	61.6	127.0	45.9	18.5	26.4	26.3	20.9	28.2	31.1	36.8	27.77
PDMS	D4	1.95	10	2.5	CYL	120.0	29.6	0	60.8	129.6	46.8	18.6	20.5	20.6	27.6	28.4	31.3	37.1	27.87
PDMS	D6	1.98	8.6$^{\sharp}$	2.5	CYL	123.0	25.8	0	58.2	124.0	46.8	19.2	26.7	25.1	30.2	28.3	31.2	36.9	24.25
NOA-61	9U	175	7.1	2	t,hCYL	53.2	70.3	30	95.5	184.3	44.0	14.4	51.7	60.1	54.6	13.6$^{\uparrow}$	12.0$^{\uparrow}$	13.3$^{\uparrow}$	32.78
NOA-61	9M	175	7.1	1.85	t,hCYL	52.8	66.4	30	97.4	185.1	43.5	15.7	51.7	60.1	54.6	13.4$^{\flat}$	13.0$^{\flat}$	14.7$^{\flat}$	30.66
JB-Weld	R10	2070	8	2	CYL	33.0	64.6	0	92.3	203.3	47.7	11.7	24.1	22.0	27.3	7.6	8.6	7.0	60.81
JB-Weld	9U	2070	7.1	2	t,hCYL	59.4	67.3	30	88.9	185.1	46.2	15.7	73.4	72.2	51.5	8.9$^{\uparrow}$	9.3$^{\uparrow}$	13.1$^{\uparrow}$	30.46
JB-Weld	9M	2070	7.1	1.85	t,hCYL	69.1	67.1	30	93.1	185.1	44.8	17.5	73.4	72.2	51.5	8.8$^{\flat}$	10.1$^{\flat}$	14.4$^{\flat}$	29.35
SiO_2/IPP	E′	6230†	6.5	2	CYL	50	10	0	38.5	73.9	43.8	12.6	17.8	-	-	17.7	-	-	9.41
SiO_2/IPP	K′	6230†	6.5	2	CYL	50	10	0	32.3	110.5	59.7	12.0	16.8	-	-	10.0	-	-	9.41
Al_2O_3/IPP	O	11260†	4	1	hCONL	39	15	21.0	40	80	45	13.4	24.9	25.1	-	13.8$^{\flat}$	19.2$^{\flat}$	-	3.85
Al_2O_3/IPP	M	11260†	4	1	hCONL	86	15	9.9	50	50	0	15.5	24.9	25.1	-	25.3$^{\uparrow}$	29.4$^{\uparrow}$	-	5.77
Al_2O_3/IPP	G	11260†	4	1	hCONL	97	15	8.8	40	80	45	18.1	24.9	25.1	-	27.3$^{\uparrow}$	31.6$^{\uparrow}$	-	3.85
Al_2O_3/IPP	H	12200†	4	1	hCONL	44	10	12.8	50	50	0	14.6	24.9	25.1	-	19.7$^{\flat}$	25.1$^{\flat}$	-	3.85

$\sharp$ - after fabrication the wicking array length was reduced to $L \approx 8.6$ mm by cutting the sample with a knife edge.

$\flat$,$\uparrow$ - calculated K-values for anisotropic sluggish climb (SC) and rapid ascent (RA) hemiwicking (respectively).

$\dagger$ - composite (or effective) Young's modulus of thin-film coated IP Photoresin (IPP) pillars (Eq. S4, Sec. S6).

Supplementary Figures

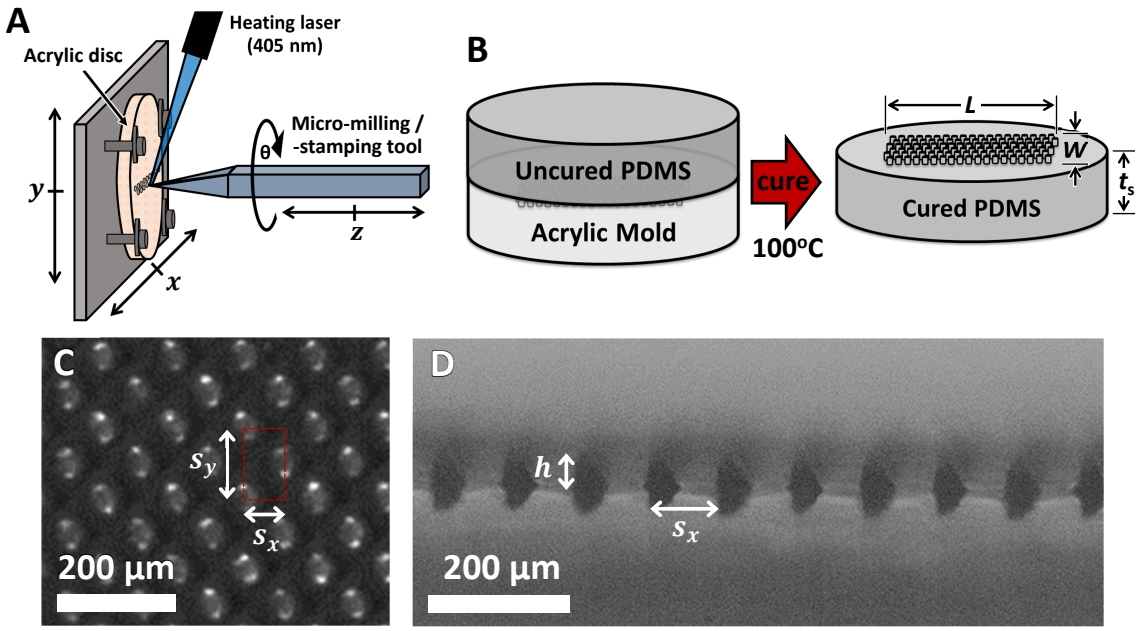

Fig. S1. Replica molding of hemiwicking samples. (***A***) Schematic depiction of the micro-milling and micro-stamping apparatus for replica negative mold fabrication. (***B***) Illustration of the replica molding process. (***C***) Top-view and (***D***) Side-view camera images for the fabricated PDMS (D2) and NOA-61 (9M) samples, respectively. The images are annotated to illustrate the s_x and s_y pillar spacing and h pillar height (see also Table S4). The cured sample thickness is typically within 2 mm $\lesssim t_s \lesssim$ 5 mm (i.e., $t_s \gg h$).

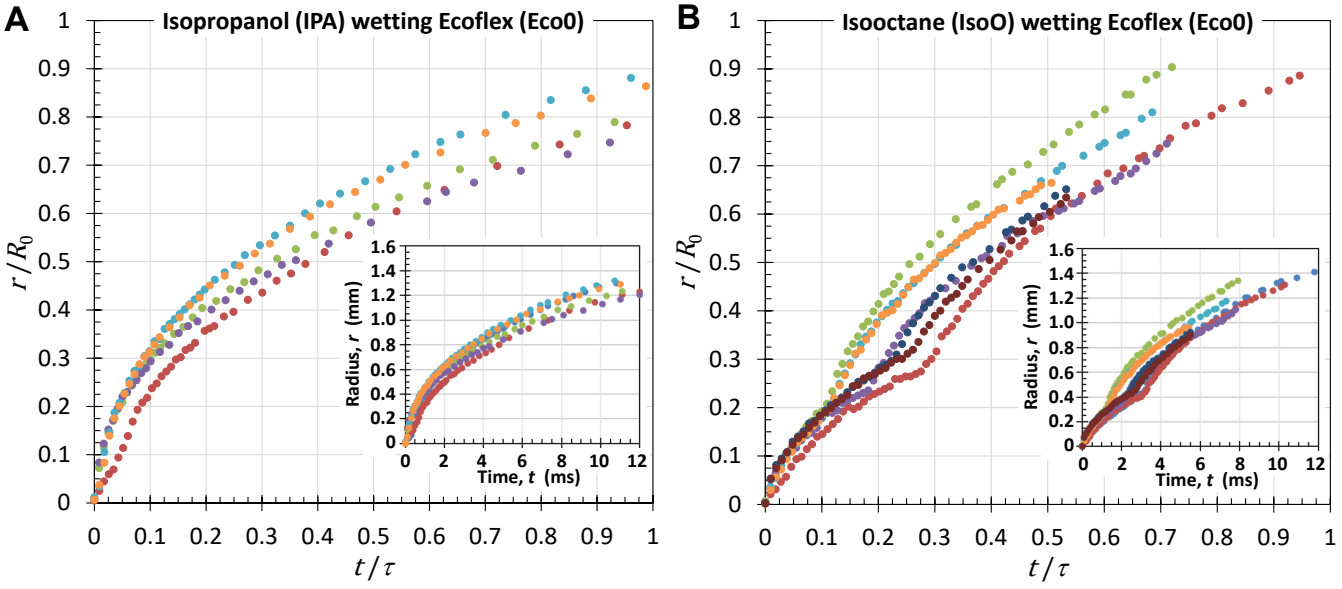

Fig. S2. Inertial-to-viscoelastic droplet wetting results. Multiple trial data for two different fluids wetting the non-textured region of the ultrasoft ($E = 61 \pm 1$ kPa) Ecoflex (Eco0) sample. (***A***) Eco0-IPA and (***B***) Eco0-IsoO sample-fluid couples. The results are plotted based on the contemporary inertial scaling (Eq. S1, Eq. 1 [manuscript]) for multiple trials with each respective fluid. The subset plots in ***A*** and ***B*** provide the non-normalized spatiotemporal wetting results. The average of these results are plotted in Fig. 1 [manuscript].

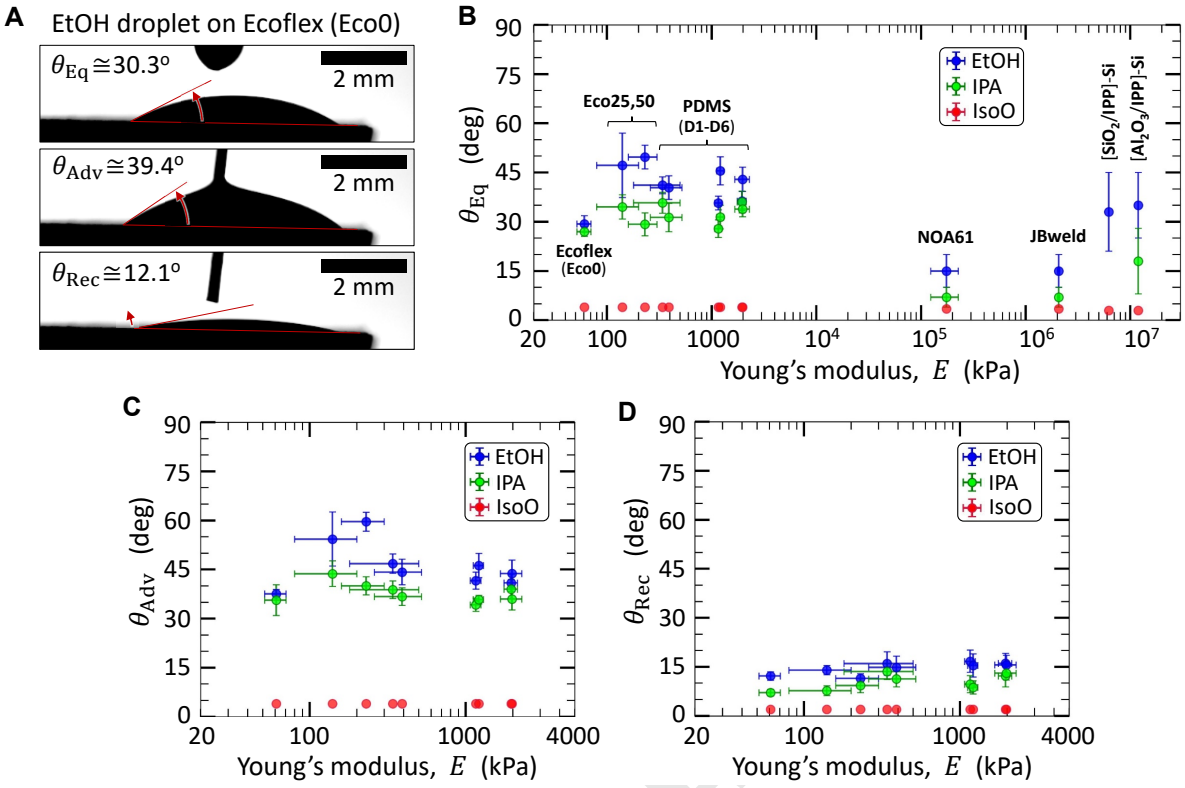

Fig. S3. Dynamic contact angle measurements. (***A***) Camera images of the static and dynamic contact angles measured for an EtOH droplet wetting the ultrasoft Ecoflex Eco0 sample. (***B***) Equilibrium (θ_{Eq}), (***C***) Advancing (θ_{Adv}), and (***D***) Receding (θ_{Rec}) contact angle results for the different sample-fluid couples studied. The results are plotted verses the measured Young's modulus (E) and are based on multiple ($N = 5 \pm 2$) trials with the different Ethanol (EtOH), Isopropanol (IPA), and Isooctane (IsoO) fluids on the non-textured surface regions of the hemiwicking samples (Table S3 provides a numeric listing of θ_{Eq} measured for these different sample-fluid couples).

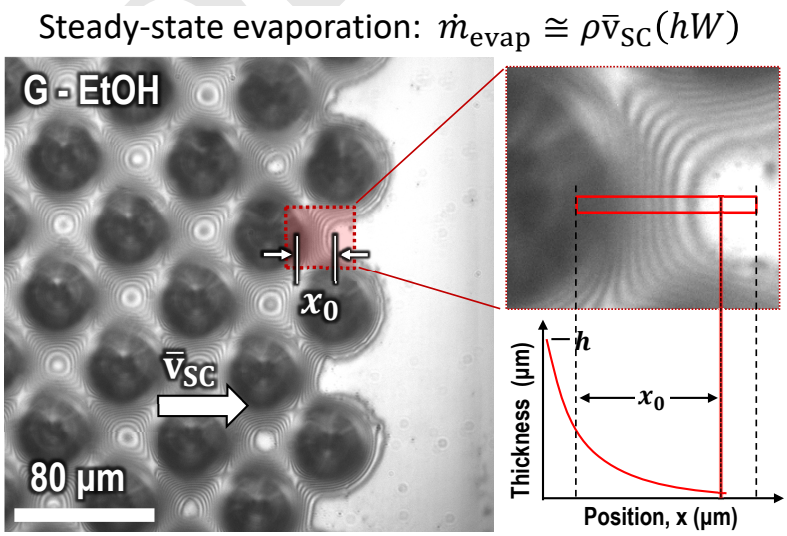

Fig. S4. Meniscus extension characterization. Illustration of measurement methodology for characterization of solid-liquid meniscus extension (x_0) during the steady-state mode of wicking array evaporation ($\dot{m}_{evap} = \dot{m}_{wick}$). The process combines standard videography with interferometry (fringe) analysis at the end of the wicking array (11). This example is for the EtOH working fluid with the anisotropic (hCONL) IPP pillars on Si (sample G, SC hemiwicking). The measured x_0 values for each sample-fluid couple are provided in Tables S3–S4 and Fig. S5.

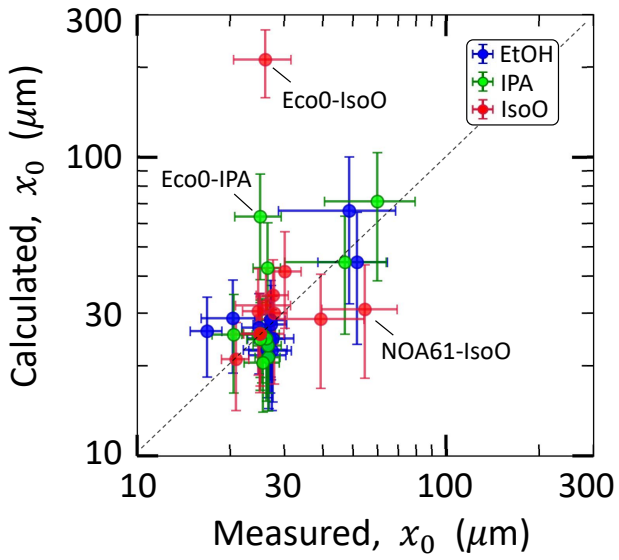

Fig. S5. Meniscus extension results. Comparison between the measured and calculated solid-liquid meniscus extension (x_0). The measured x_0 results are based on the steady-state meniscus evaporation measurement methodology (Fig. S4), whereas the calculated x_0 results are based on Eq. S2a (or Eq. 2 [manuscript]), using $\hat{\mathrm{v}}_{\mathrm{wet}}$ and θ_{Eq} independently measured for each sample-fluid couple (Supplementary Text S2–S4). Aside from the ultrasoft Ecoflex (Eco0) and the anisotropic NOA61 samples, a good correlation is found for all sample-fluid couples. The measured x_0, θ_{Eq}, and $\hat{\mathrm{v}}_{\mathrm{wet}}$ results (along with the E for each sample) are also provided in Table S3.

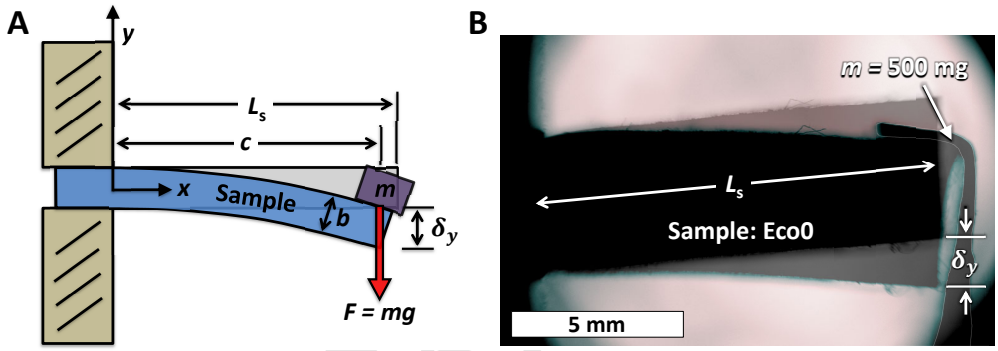

Fig. S6. Young's modulus characterization. (***A***) Schematic depiction of sample/beam deflection setup for Young's modulus (E) measurements (Eq. S3). (***B***) Image overlay measurement methodology. Camera images before and after sample deflection are overlaid to optically measure the $\delta_{\hat{y}}$ defection for a given applied mass. The example provided is a measurement trial with the ultrasoft Ecoflex (Eco0) sample, using an applied ≈500 mg mass coupon at the end of the clamped sample. Trial results: $E = 62.4 \pm 7.7$ kPa, where $\delta_{\hat{y}} = 1.45 \pm 0.06$ mm, $L_{\mathrm{s}} = 11.79 \pm 0.08$ mm (length), $c \approx L_{\mathrm{s}}$, $a = 4.90 \pm 0.08$ mm (width), and $b = 4.17 \pm 0.06$ mm (thickness).

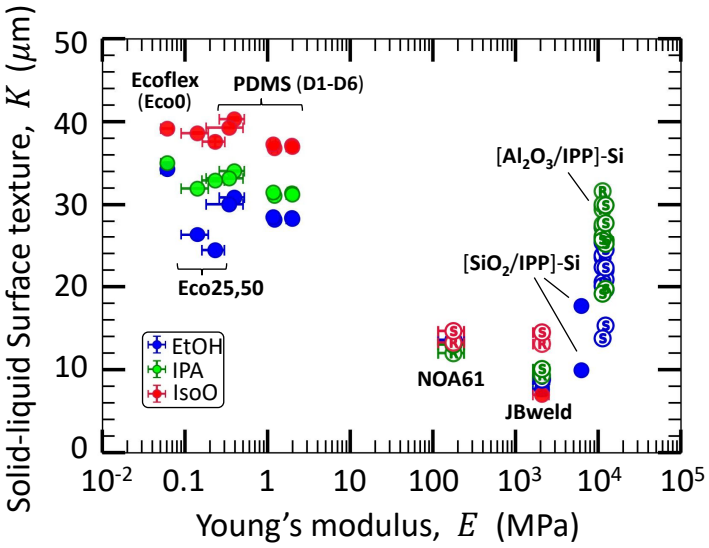

Fig. S7. Solid-liquid Surface textures. Predicted solid-liquid Surface textures K (Eq. S9, Eq. 4 [manuscript]) plotted as a function of the measured Young's modulus for each sample-fluid couple tested. The filled symbols represent the corresponding K values for the isotropic hemiwicking samples (CYL pillar arrays), whereas the annotated 'S' and 'R' symbols represent the calculated K values for the anisotropic t,hCYL or hCONL pillar arrays in the 'sluggish climb' (SC) and 'rapid ascent' (RA) hemiwicking configurations (respectively).

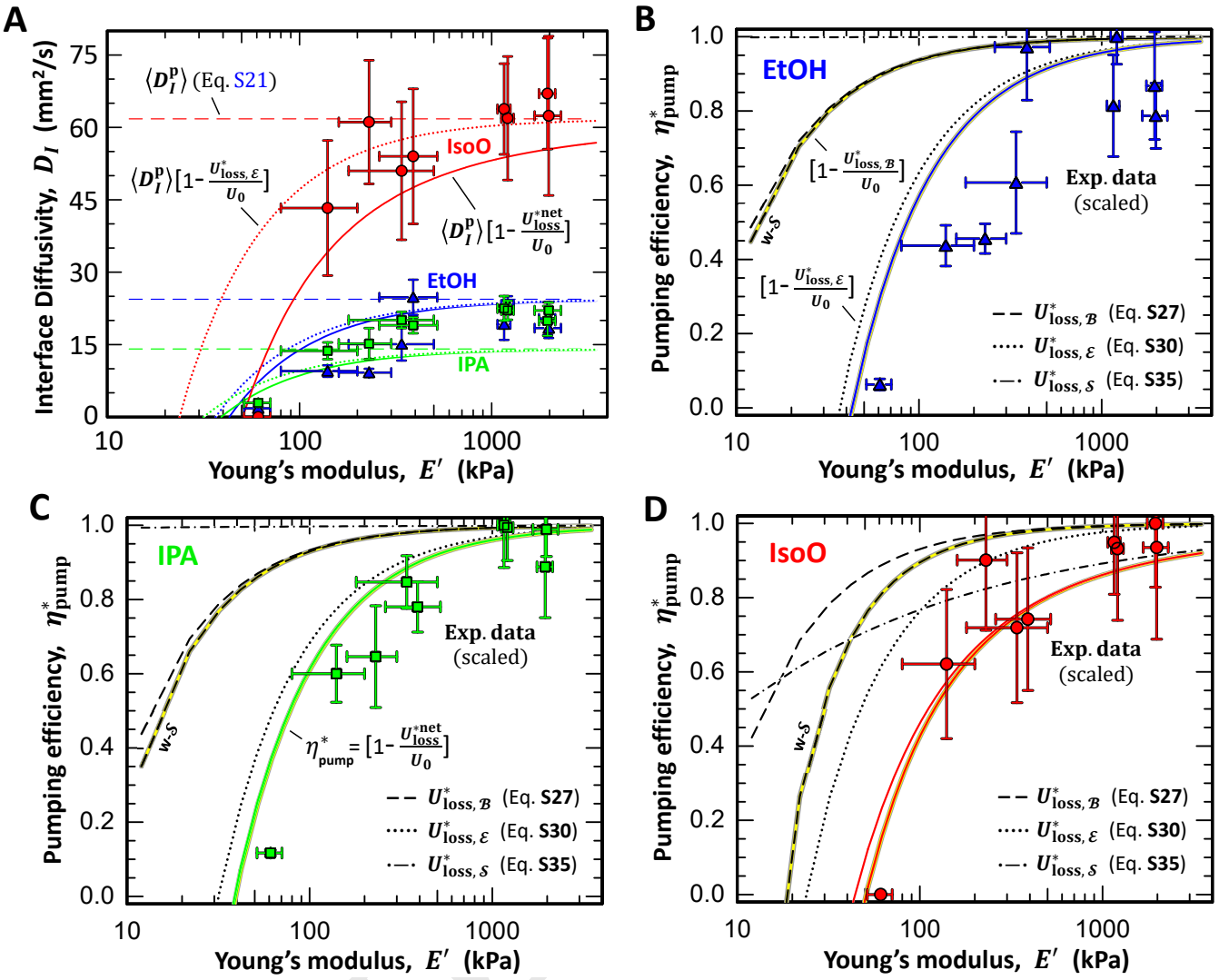

Fig. S8. Effects of viscoelastic dissipation on the meniscus interface diffusivity. Predicted dissipation in the hemiwicking pumping energy (per unit wicking cell) due to the individual or combined effects of inelastic pillar deflections ($U^*_{\text{loss},\mathcal{B}}$), propagating elastocapillary surface deformations ($U^*_{\text{loss},\mathcal{E}}$), and spatiotemporal swelling of the micropillars ($U^*_{\text{loss},\mathcal{S}}$). (***A***) Dissipation analysis based on the measured (symbols) and predicted (lines) meniscus interface diffusivity for the different systems studied as a function of the dry state Young's modulus of the wicking array. The solid- and dashed-line predictions abide with Eq. S24 and Eq. S21, where $\eta^*_{\text{pump}} = 1 - U^{*,\text{net}}_{\text{loss}}/U_0$ is the net reduction in the capillary pumping energy (per unit wicking cell) due to these three different viscoelastic loss mechanisms. (***B–D***) Predicted dissipation in the hemiwicking pumping efficiency based on the different loss mechanisms for each respective EtOH, IPA, and IsoO working fluid. The predictions are compared to the experimental results for each sample-fluid couple, where the measured $\bar{D}_I$ results in (*A*) have been normalized in (*B–D*) for respective comparisons to η^*_{pump} predicted. The highlighted (yellow) line predictions represent the expected enhancements in $U^*_{\text{loss},\mathcal{B}}$ and $U^{*,\text{net}}_{\text{loss}}$ due to swelling-induced softening of the micropillars (Eq. S44). The *model parameters* and *sample-fluid properties* used are $\bar{h} = 127.41\,\mu$m, $\bar{r}_p = 26.88\,\mu$m, $\bar{s}_x = 60.59\,\mu$m, $\bar{s}_y = 127.44\,\mu$m, $\bar{\theta}^{\text{EtOH}}_{\text{Eq}} = 40.9°$, $\bar{\theta}^{\text{IPA}}_{\text{Eq}} = 31.9°$, $\bar{\theta}^{\text{IsoO}}_{\text{Eq}} = 5°$, $\mathcal{S}^{\text{EtOH}}_r = 1.04$, $\mathcal{S}^{\text{IPA}}_r = 1.09$, $\mathcal{S}^{\text{IsoO}}_r = 1.35$, $t_{\text{wet}} = 20$ ms, $\bar{\nu} = 0.47$, $\tan\bar{\varphi} = 0.25$, and $E_\star = 1$ MPa (see, Tables S1–S4 and Fig. S9).

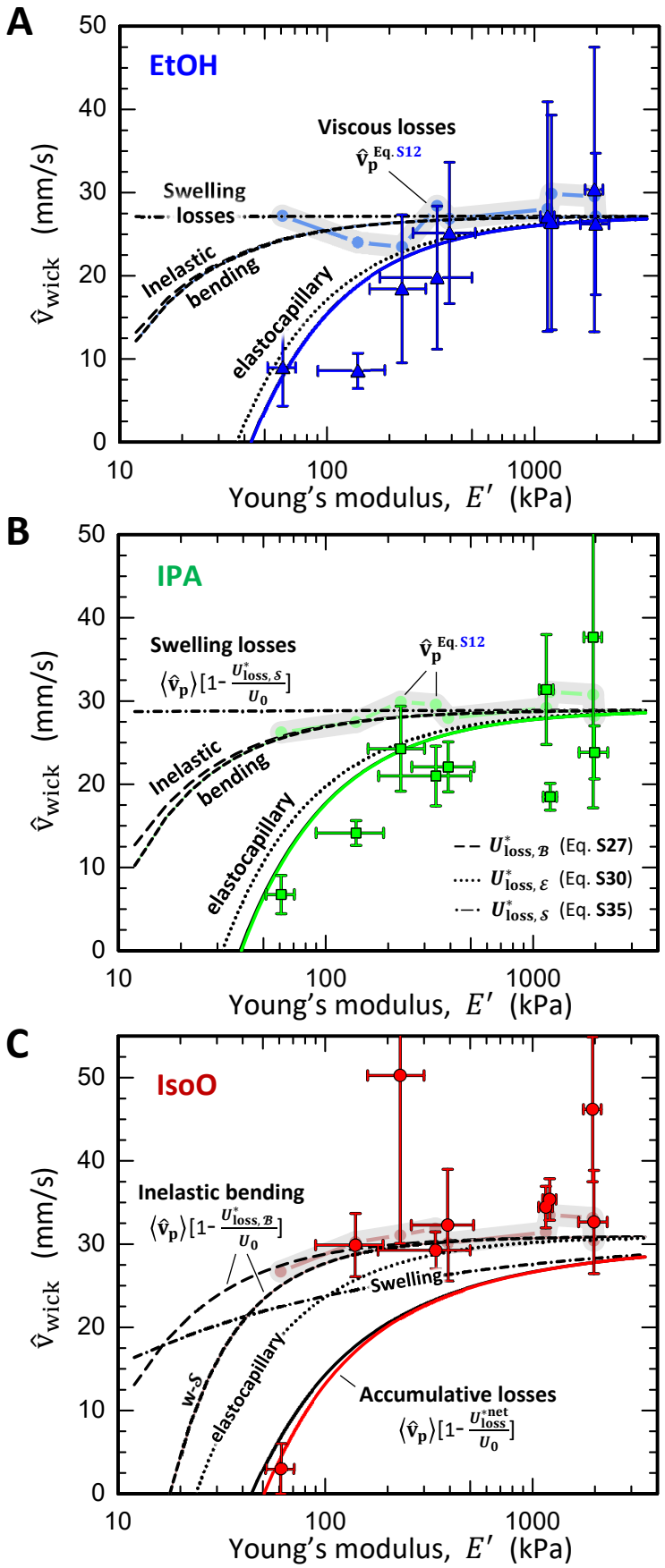

Fig. S9. Effects of viscoelastic dissipation on the maximum hemiwicking velocity. Comparison between the measured (symbols) and predicted (lines) maximum hemiwicking $\hat{v}_{wick}$ velocity as a function of the initial dry state elastic E' modulus of the wicking array. (***A***–***C***) results for the ethanol (EtOH), isopropanol (IPA), and Isooctane (IsoO) working fluids, respectively. The line predictions show the individual and accumulative effects of the viscoelastic losses on the hemiwicking pumping efficiency – i.e., $\hat{v}_{wick} = \langle\hat{v}_p\rangle\,\eta^*_{pump}$, where $\langle\hat{v}_p\rangle$ is the average wicking velocity predicted by Eq. S12 for developed hemiwicking flow at $\ell = \ell_e$ that accounts for viscous drag with the pillar walls and $\eta^*_{pump} = 1 - U^*_{loss,i}/U_0$ is the pumping efficiency that accounts for viscoelastic losses from inelastic pillar deflections ($U^*_{loss,\mathcal{B}}$), propagating elastocapillary wetting ridge deformations ($U^*_{loss,\mathcal{E}}$), or spatiotemporal swelling of the micropillars ($U^*_{loss,\mathcal{S}}$) relative to the maximum pumping U_0 potential per unit wicking cell. The gray-shaded circle symbols represent $\hat{v}_p$ calculated with Eq. S12 (and supporting Eq. S2a, S11a, and S13) for each individual sample-fluid couple, whereas $\langle\hat{v}_p\rangle$ is predicted average for a given fluid with these different Ecoflex–PDMS wicking arrays. Likewise, our $U^*_{loss,i}$ calculations use averaged modeling conditions and sample-fluid properties (e.g., $\bar{h} = 127.41\,\mu$m, $\bar{r}_p = 26.88\,\mu$m, $\bar{s}_x = 60.59\,\mu$m, $\bar{s}_y = 127.44\,\mu$m, $\bar{\theta}^{EtOH}_{Eq} = 40.9°$, $\bar{\theta}^{IPA}_{Eq} = 31.9°$, $\bar{\theta}^{IsoO}_{Eq} = 5°$, $\mathcal{S}^{EtOH}_r = 1.04$, $\mathcal{S}^{IPA}_r = 1.09$, $\mathcal{S}^{IsoO}_r = 1.35$, $t_{wet} = 20$ ms, $\bar{\nu} = 0.47$, $\tan\hat{\varphi} = 0.25$, and $E_\star = 1$ MPa; see, Tables S1–S4).

Movie captions

Movie S1 (caption): Hemiwicking results for Isooctane (IsoO) and several different wicking arrays with Young's moduli ranging from ∼140 kPa to ∼2.07 GPa. The key result demonstrated is that real-time (transient) pillar clustering (induced by the IsoO working fluid with the soft Eco25 and Eco50 wicking arrays) does not significantly reduce the overall wicking performance - relative to the other PDMS (D3, D2, and D4) samples with nearly identical wicking array geometries (Table S3 and S4). However, if the stiffness (E) of the wicking array is $\lesssim$140 kPa, then hemiwicking in the wicking array can be completely suppressed (i.e., the ultrasoft ($\sim$61 kPa) Ecoflex sample did not hemiwick with IsoO). Thus, given that $E \gtrsim 140$ kPa, changes in sample surface chemistry, pillar spacing configuration, and pillar geometry are more important than changes in sample stiffness (NOA61 and JBweld results). These results also demonstrate the importance of maximizing the hydraulic radius of the wicking array (or hydraulic radius of the unit wicking cell) for open-channel hemiwicking flow while maintaining a pillar spacing configuration with pillar separations on the same order of the meniscus extension (i.e., $s_\kappa < x_0$ is detrimental and $s_\kappa \gg x_0$ will completely quench the hemiwicking process). Scale bars (blue): 1 mm (in width).

Movie S2 (caption): High-speed camera videos (11001 fps) for the onset of hemiwicking with the soft (∼140 kPa) Eco25 wicking array. The initial wetting and hemiwicking data is provided for all three working fluids tested (EtOH, IPA, and IsoO). The displayed videography data is within the cropped region-of-interest (ROI) indicated in Fig. 5*A* [manuscript]. The center video/image also displays (for reference) the unit wicking cell for this wicking array. The key results demonstrated are that real-time (transient) pillar deflections are observed for all three working fluids; however, only the IsoO working fluid induces the clustering of pillars during the hemiwicking process. While the other (EtOH and IPA) working fluids induce pillar deflections in the range 5 μm $\lesssim \delta \lesssim$ 20 μm, the magnitude of these pillar deflections are not enough to induce clustering. Tables S3 and S4 provide additional sample characteristics/properties, where the Eco25 sample is 75% Ecoflex and 25% PDMS (by mass).

Legend: Fig. 4*A*–*F* and Fig. 7*A*–*C* [manuscript]

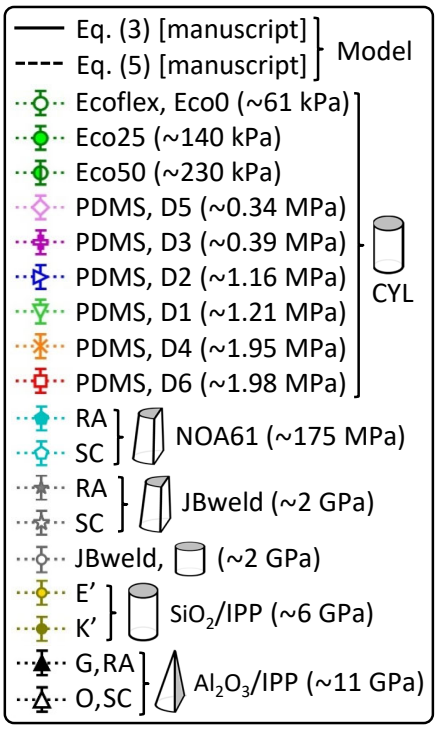

(Left) Legend for hemiwicking data (symbols) and predictions (lines) for Fig. 4*A-F* and Fig. 7*A-C* [manuscript].

Also provided below are illustrations of the different hemiwicking configurations: (***A***) isotropic hemiwicking with symmetric cylindrical (CYL) pillars and (***B,C***) anisotropic hemiwicking with asymmetric half-conical (hCONL) pillars in the faster rapid ascent (RA) or slower sluggish climb (SC) pillar orientations (respectively).

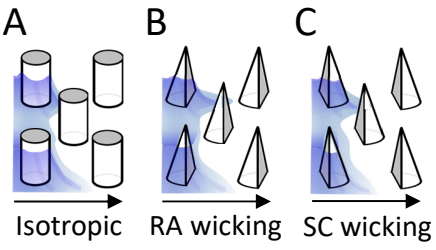

Nomenclature

A, A_F	area, frontal area, [m^2]
B	bending modulus, [Pa]
D_I	meniscus interface diffusivity, [m^2/s]
$D_{\mathcal{S}}$	solvent swelling diffusivity, [m^2/s]
E	Young's modulus (or elastic modulus), [Pa]
f	force per unit wicking cell width, [N/m]
g	gravitational acceleration, [m/s^2]
G	shear modulus, [Pa]
h	pillar height, [m]
I_x, I_y	area moments of inertia of cross section, [m^4]
K	solid-liquid Surface texture, [m]
ℓ	meniscus propagation length, [m]
ℓ_e	entrance length, [m]
L	length (wicking array, structure, sample), [m]
L_c	characteristic length, [m]
P	pressure, [Pa]
$\mathcal{P}$	perimeter length, [m]
r	radius or radial displacement, [m]
r_p	pillar radius (at base $\perp$ to flow), [m]
R	droplet radius (or radius of curvature), [m]
R_h	hydraulic radius, [m]
s_x, s_y	wicking cell dimensions, [m]
s_κ	inter-pillar (wall-to-wall) distance, [m]
t	time, [sec] or thickness, [m]
U_0	capillary pumping energy (per wicking cell), [J]
U_{loss}	pumping energy dissipated, [J]
v	velocity, [m/s]
$V, \dot{V}$	volume, volume flow rate, [m^3, m^3/s]
w_0	capillary bridge width, [m]
$\bar{w}$	average load distribution, [N/m]
W	width (wicking array, structure, sample), [m]
x_0	meniscus extension (steady-state), [m]
$\mathcal{S}_r$	swelling ratio, [%]

Subscripts & Superscripts

Adv	advancing
c	characteristic or cross-sectional
cr	critical
Eq	equilibrium
exp	experiment or experimental
f	film, thin-film, or fluid
max	maximum
ocf	open channel flow
onset	onset of a process
p, p	pillar, predicted
Rec	receding
$\mathcal{S}, \mathcal{E}, \mathcal{B}$	Swelling, Elastocapillary, Bending
w, wet	wet & wetting
wick	wick & wicking
x, y, z	x-, y-, or z-axis

Greek

α	wicking cell pillar offset angle, [deg]
β	pillar wall slant angle, [deg]
γ	surface tension, [N/m]
δ	pillar/beam deflection length, [m]
ϵ	strain, $\epsilon = \Delta\mathrm{x}/\mathrm{x}$
η	efficiency
θ	contact angle, [deg]
κ	curvature (meniscus or fluid-film), [1/m]
μ	dynamic viscosity, [Pa·s]
ν	Poisson's ratio
Π	Osmotic pressure, [Pa]
ρ	density, [g/cm^3]
τ	timescale, [sec]
ϕ	area or volume fraction
Ω_s	volume per solvent molecule, [m^3]

Characteristic or Dimensionless quantities

Ca	capillary number, $\mathrm{Ca} = (\mu/\gamma)\mathrm{v}$
C_{d0}	Stokes drag coefficient, $C_{d0} = 24$
l_{bc}	bendocapillary length [m]
l_{ec}	elastocapillary length [m], $l_{\mathrm{ec}} = \gamma/G$
N, n	number
Re	Reynolds number, $\mathrm{Re} = \rho \mathrm{v} L_c/\mu$
S	solid-liquid Structure factor, $S = K/\ell$
We	Weber number, $\mathrm{We} = \rho \mathrm{v}^2 L_c/\gamma$
$\tan\varphi$	loss tangent, $\tan\varphi = E''/E'$

Acronyms

Eco0	Ecoflex (platinum-catalyzed silicone)
Eco25	75% Ecoflex, 25% PDMS (by mass)
Eco50	50% Ecoflex, 50% PDMS (by mass)
EtOH	Ethanol (Ethyl alcohol)
fps	frames per second, [#/s]
EtOH	Ethanol (Ethyl alcohol)
IPA	Isopropanol (Isopropyl alcohol)
IPP	IP Photoresin
IsoO	Isooctane (2,2,4-Trimethylpentane)
JBweld	J-B Weld two-part epoxy adhesive
NOA	Norland Optical Adhesive
PDMS	Polydimethylsiloxane
RA	rapid ascent (wicking convention)
ROI	Region of Interest
SC	sluggish climb (wicking convention)

Common Accents (x, *variable)*

$\hat{\mathrm{x}}$	apex or maximum value
$\bar{\mathrm{x}}$	average (or length-weighted) value
$\dot{\mathrm{x}}$	time derivative of variable
$\mathrm{x}', \mathrm{x}''$	real, imaginary (loss) contribution

Acknowledgments. This material is based on research primarily sponsored by the National Science Foundation (Grant No. 1653396). The research was also partially sponsored by the U.S. Office of Naval Research (Grant No. N0001415-1-2481). The views and conclusions contained herein are those of the authors and should not be interpreted as necessarily representing the official policies or endorsements, either expressed or implied, of U.S. Government (and/or departments thereof). 3D printing and fabrication of a subset of hemiwicking samples was conducted as part of a user project at the Center for Nanophase Material Sciences (User Proposals: CNMS2017-R51 and CNMS2018-329), which is a US Department of Energy, Office of Science User Facility at Oak Ridge National Laboratory (ORNL). The authors gratefully acknowledge the fruitful discussions with Ranjay Ghosh and Yuanli Bai and experimental assistance from Bernadeta R. Srijanto and Nick Lavrik at ORNL and K.S.R. Manoharan, J. Bal, C. Brewer, M. Gomez, J. Carter, and T. Chowdhury at UCF.

References

1. Germain T, Brewer C, Scott J, Putnam SA (2018) Scalable stamp printing and fabrication of hemiwicking surfaces. *JoVE (Journal of Visualized Experiments)* (142):e58546.
2. Khanafer K, Duprey A, Schlicht M, Berguer R (2009) Effects of strain rate, mixing ratio, and stress–strain definition on the mechanical behavior of the polydimethylsiloxane (pdms) material as related to its biological applications. *Biomedical microdevices* 11(2):503.
3. Wildeman S, Visser CW, Sun C, Lohse D (2016) On the spreading of impacting drops. *Journal of Fluid Mechanics* 805:636–655.
4. Chen L, Bonaccurso E, Deng P, Zhang H (2016) Droplet impact on soft viscoelastic surfaces. *Physical Review E* 94(6):063117.
5. Courbin L, Bird JC, Reyssat M, Stone HA (2009) Dynamics of wetting: from inertial spreading to viscous imbibition. *Journal of Physics: Condensed Matter* 21(46):464127.
6. Biance AL, Clanet C, Quéré D (2004) First steps in the spreading of a liquid droplet. *Physical Review E* 69(1):016301.
7. Winkels KG, Weijs JH, Eddi A, Snoeijer JH (2012) Initial spreading of low-viscosity drops on partially wetting surfaces. *Physical Review E* 85(5):055301.
8. Eddi A, Winkels KG, Snoeijer JH (2013) Short time dynamics of viscous drop spreading. *Physics of fluids* 25(1):013102.
9. Culick FEC (1960) Comments on a ruptured soap film. *Journal of Applied Physics* 31(6):1128–1129.
10. Thoroddsen ST, Etoh TG, Takehara K, Ootsuka N (2005) On the coalescence speed of bubbles. *Physics of Fluids* 17(7):071703.
11. Arends AA, Germain TM, Owens JF, Putnam SA (2018) Simultaneous reflectometry and interferometry for measuring thin-film thickness and curvature. *Review of Scientific Instruments* 89(5):055117.
12. Krishnan SR, Bal J, Putnam SA (2019) A simple analytic model for predicting the wicking velocity in micropillar arrays. *Scientific Reports* 9(1):1–9.
13. Bal J, Manoharan KS, Putnam SA (2021) Spatiotemporal wicking dynamics: The effects of pillar height, density, and anisotropic geometries in *2021 20th IEEE Intersociety Conference on Thermal and Thermomechanical Phenomena in Electronic Systems (ITherm)*. (IEEE), p. 1214.
14. Rossi S, Bergamo L, Calovi M, Fontanari V (2019) Effect of enamel coatings on the mechanical properties of aluminium foams. *Mechanics of Advanced Materials and Structures* 26(13):1130–1139.
15. Kim J, Moon MW, Kim HY (2016) Dynamics of hemiwicking. *Journal of Fluid Mechanics* 800:57–71.
16. Bico J, Thiele U, Quéré D (2002) Wetting of textured surfaces. *Colloids and Surfaces A: Physicochemical and Engineering Aspects* 206(1):41–46.
17. Ishino C, Reyssat M, Reyssat E, Okumura K, Quéré D (2007) Wicking within forests of micropillars. *Euro Physics Letters* 79(5):56005.
18. Srivastava N, Din C, Judson A, MacDonald NC, Meinhart CD (2010) A unified scaling model for flow through a lattice of microfabricated posts. *Lab Chip* 10(9):1148–1152.
19. Xiao R, Enright R, Wang EN (2010) Prediction and optimization of liquid propagation in micropillar arrays. *Langmuir* 26(19):15070–15075. PMID: 20806979.
20. Natarajan B, et al. (2021) Predicting hemiwicking dynamics on textured substrates. *Langmuir* 37(1):188–195. PMID: 33347296.
21. Mesbahi AH, Germain T, Patel PK, Putnam SA, Chumbimuni-Torres KY (2022) Tuning the fluid wetting dynamics on gold microstructures using photoactive compounds. *Applied Surface Science* 589:152924.
22. Flory PJ, Rehner, John J (1943) Statistical mechanics of cross-linked polymer networks ii. swelling. *The Journal of Chemical Physics* 11(11):521–526.
23. Flory PJ (1944) Network structure and the elastic properties of vulcanized rubber. *Chemical Reviews* 35(1):51–75.
24. Flory PJ (1950) Statistical mechanics of swelling of network structures. *The Journal of Chemical Physics* 18(1):108–111.
25. Ha J, Kim HY (2020) Capillarity in soft porous solids. *Annual Review of Fluid Mechanics* 52(1):263–284.
26. Schoen I, Hu W, Klotzsch E, Vogel V (2010) Probing cellular traction forces by micropillar arrays: Contribution of substrate warping to pillar deflection. *Nano Letters* 10(5):1823–1830.
27. Rubino E, Ioppolo T (2016) Young's modulus and loss tangent measurement of polydimethylsiloxane using an optical lever. *Journal of Polymer Science Part B: Polymer Physics* 54(7):747–751.
28. Xu S, Zhou Z, Liu Z, Sharma P (2023) Concurrent stiffening and softening in hydrogels under dehydration. *Science Advances* 9(1):eade3240.
29. Cai Z, Skabeev A, Morozova S, Pham JT (2021) Fluid separation and network deformation in wetting of soft and swollen surfaces. *Communications Materials* 2(1):21.
30. Yu Ys (2012) Substrate elastic deformation due to vertical component of liquid-vapor interfacial tension. *Applied Mathematics and Mechanics* 33(9):1095–1114.
31. Style RW, Jagota A, Hui CY, Dufresne ER (2017) Elastocapillarity: Surface tension and the mechanics of soft solids. *Annual Review of Condensed Matter Physics* 8:99–118.
32. Style RW, et al. (2013) Universal deformation of soft substrates near a contact line and the direct measurement of solid surface stresses. *Phys. Rev. Lett.* 110(6):066103.
33. Gerber J, Lendenmann T, Eghlidi H, Schutzius TM, Poulikakos D (2019) Wetting transitions in droplet drying on soft materials. *Nature Communications* 10(1):4776.
34. Bico J, Reyssat E, Roman B (2018) Elastocapillarity: When surface tension deforms elastic solids. *Annual Review of Fluid Mechanics* 50(1):629–659.
35. Andreotti B, Snoeijer JH (2020) Statics and dynamics of soft wetting. *Annual Review of Fluid Mechanics* 52(1):285–308.
36. Choi J, et al. (2021) Skin-interfaced microfluidic systems that combine hard and soft materials for demanding applications in sweat capture and analysis. *Advanced Healthcare Materials* 10(4):2000722.
37. Pandey A, Holmes DP (2013) Swelling-induced deformations: a materials-defined transition from macroscale to microscale deformations. *Soft Matter* 9(23):5524–5528.
38. Tanaka T, Fillmore DJ (1979) Kinetics of swelling of gels. *The Journal of Chemical Physics* 70(3):1214–1218.
39. Bouklas N, Huang R (2012) Swelling kinetics of polymer gels: comparison of linear and nonlinear theories. *Soft Matter* 8(31):8194–8203.
40. Yoon J, Cai S, Suo Z, Hayward RC (2010) Poroelastic swelling kinetics of thin hydrogel layers: comparison of theory and experiment. *Soft Matter* 6(23):6004–6012.
41. Chen S, Huang R, Ravi-Chandar K (2020) Linear and nonlinear poroelastic analysis of swelling and drying behavior of gelatin-based hydrogels. *International Journal of Solids and Structures* 195:43–56.
42. Abney JR, Scalettar BA, Owicki JC (1989) Mutual diffusion of interacting membrane proteins. *Biophys J* 56(2):315–326.
43. Kang MK, Huang R (2010) A Variational Approach and Finite Element Implementation for Swelling of Polymeric Hydrogels Under Geometric Constraints. *Journal of Applied Mechanics* 77(6). 061004.
44. Shanmuganathan K, Capadona JR, Rowan SJ, Weder C (2010) Stimuli-responsive mechanically adaptive polymer nanocomposites. *ACS Applied Materials & Interfaces* 2(1):165–174. PMID: 20305827.
45. Lee JN, Park C, Whitesides GM (2003) Solvent compatibility of poly(dimethylsiloxane)-based microfluidic devices. *Analytical Chemistry* 75(23):6544–6554. PMID: 14640726.
46. Binysh J, Wilks TR, Souslov A (2022) Active elastocapillarity in soft solids with negative surface tension. *Science Advances* 8(10):eabk3079.
47. Burke J (1984) Solubility parameters: Theory and application, (AIC Book and Paper Group Annual, Vol. 3), Technical report.
48. Hansen CM (2007) *Hansen solubility parameters: a user's handbook*. (CRC press).
49. Huang J, et al. (2020) Wrinkle-enabled highly stretchable strain sensors for wide-range health monitoring with a big data cloud platform. *ACS Applied Materials & Interfaces* 12(38):43009–43017. PMID: 32856459.
50. Moučka R, Sedlačík M, Osička J, Pata V (2021) Mechanical properties of bulk sylgard 184 and its extension with silicone oil. *Scientific Reports* 11(1):19090.